nature communications

Article

https://doi.org/10.1038/s41467-025-57484-4

Microbiome-emitted scents activate olfactory neuron-independent airway-gut-brain axis to promote host growth in *Drosophila*

Received: 13 June 2024

Accepted: 13 February 2025

Published online: 04 March 2025

Check for updates

Jin-Woo Lee[1,8], Kyung-Ah Lee[1,2,8], In-Hwan Jang[1], Kibum Nam[1], Sung-Hee Kim[1], Minsoo Kyung[1], Kyu-Chan Cho[1], Ji-hoon Lee[1], Hyejin You[1], Eun-Kyoung Kim[1], Young Hoon Koh[3], Hansol Lee[3], Junsun Park[1], Soo-Yeon Hwang[4], Youn Wook Chung[5], Choong-Min Ryu[6], Youngjoo Kwon[4], Soung-Hun Roh[1,3], Ji-Hwan Ryu[5] & Won-Jae Lee[1,3,7]

While it is now accepted that the microbiome has strong impacts on animal growth promotion, the exact mechanism has remained elusive. Here we show that microbiome-emitted scents contain volatile somatotrophic factors (VSFs), which promote host growth in an olfaction-independent manner in *Drosophila*. We found that inhaled VSFs are readily sensed by olfactory receptor 42b non-neuronally expressed in subsets of tracheal airway cells, enteroendocrine cells, and enterocytes. Olfaction-independent sensing of VSFs activates the airway-gut-brain axis by regulating Hippo, FGF and insulin-like growth factor signaling pathways, which are required for airway branching, organ oxygenation and body growth. We found that a mutant microbiome that did not produce (2R,3R)-2,3-butanediol failed to activate the airway-gut-brain axis for host growth. Importantly, forced inhalation of (2R,3R)-2,3-butanediol completely reversed these defects. Our discovery of contact-independent and olfaction-independent airborne interactions between host and microbiome provides a novel perspective on the role of the airway-gut-brain axis in microbiome-controlled host development.

The co-evolution of the microbiome in animal hosts affects diverse aspects of the host physiology, including immunity, development, metabolism, and behavior[1–5]. Although many important studies demonstrate the physiological importance of gut microbiome, the lack of a genetic model of "animal-microbiome interaction" has limited the discovery of many important hidden connections between microbiome and host. The *Drosophila*–microbiome interaction model has proven to be the model of choice due to the advanced genetic toolbox for both major commensal bacteria and host animals[6–10]. Previously, in a *Drosophila* model of malnutrition, we and others found that two principal members of the *Drosophila* gut microbiome, *Acetobacter pomorum* (AP) and *Lactiplantibacillus plantarum* (LP), are required for enhanced host growth and development[11,12]. Importantly, the growth-promoting effect of these commensal bacteria is observed only under

[1]School of Biological Sciences, Seoul National University, Seoul, South Korea. [2]Saeloun Bio Inc., Seoul, South Korea. [3]Institute of Molecular Biology and Genetics, Seoul National University, Seoul, South Korea. [4]College of Pharmacy, Graduate School of Pharmaceutical Sciences, Ewha Womans University, Seoul, South Korea. [5]Severance Biomedical Science Institute, Graduate School of Medical Science, Yonsei University College of Medicine, Seoul, South Korea. [6]Molecular Phytobacteriology Laboratory, Infectious Disease Research Center, KRIBB, Daejeon, South Korea. [7]Wide River Institute of Immunology, Seoul National University, Hongcheon, South Korea. [8]These authors contributed equally: Jin-Woo Lee, Kyung-Ah Lee. e-mail: lwj@snu.ac.kr

conditions of protein malnutrition[11,12], indicating the existence of a link among microbiome, nutrition, and host growth. In both commensal bacteria, microbe-induced host growth is mediated by the activation of insulin and insulin-like growth factor (IGF) signaling in *Drosophila*[11,12].

Strikingly, a specific strain of LP originally isolated from *Drosophila* gut (LP^{WJL}) was found to enhance the juvenile growth not only in a *Drosophila* model but also in a gnotobiotic mouse model[13,14]. LP^{WJL} was shown to increase IGF-1 levels, partially via NOD2-dependent bacterial cell wall sensing, indicating evolutionarily conserved interactions between LP^{WJL} and host somatotrophic signaling pathway (e.g., IGF signaling)[13,14]. However, to date, some long-standing unanswered questions in the field are: "Which bacterial metabolic pathways, more specifically which bacterial metabolites, are capable of inducing host systemic growth?"; "How does host sense (i.e., which organs and which receptors) these microbiome-derived signals?"; and "How does host coordinate microbiome-to-organ-to-organ interactions to achieve systemic growth?". Research in this direction is of paramount importance in unraveling an unexplained association between the microbiome and the development of a malnourished host.

The present study aimed to identify microbiome-derived growth factors capable of promoting host growth, and understand the molecular mechanism by which these factors impact host physiology. We found that LP^{WJL} emits air-diffusible volatile somatotrophic factors (VSFs) that activate the airway-gut-brain axis in an olfaction-independent manner for host growth under malnutrition. Further, by identifying the chemical nature of VSFs and their cellular receptors, we found that the VSF-activated airway-gut-brain axis involves complex inter-organ signaling interactions including Hippo signaling, FGF-FGFR signaling, peptide hormone signaling, and IGF signaling pathways. Our discovery of airborne interactions involving the microbiome and different organs may provide essential clues to understanding the role of the microbiome in metazoan development during prokaryote-eukaryote co-evolution.

Results

Microbiome-emitted scents promote host growth in an olfaction-independent manner

We initially investigated the microbiome-derived growth-stimulating factors using LP^{WJL}, a well-known *Drosophila*–microbiome member capable of inducing host growth in a malnutrition-induced stunting model of *Drosophila* and rodent[11–14]. By analyzing the effects of different microbial factors on host growth using a germ-free *Drosophila* model, we made a serendipitous observation in which LP^{WJL} induced the growth of germ-free animals even without gut colonization (i.e., inhalation of LP^{WJL} volatiles in the absence of physical contact between microbes and host cells), albeit less effective than LP^{WJL} association (Fig. 1a, b). This surprising observation prompted us to hypothesize that LP^{WJL}-emitted scents contain VSFs and that airborne transmission of VSFs promotes host growth.

To ascertain whether the growth gain induced by VSF is not solely attributable to VSF's stimulation of larval feeding behavior, we compared food intake between VSF-exposed and non-exposed larvae. Given that larvae exposed to VSF for longer than 72 h after egg laying (AEL) are larger in size (e.g., larvae at 96 h AEL) than the non-exposed control larvae, thus exhibiting higher food intake (Fig. 1c), we measured food intake when VSF-exposed and non-exposed larvae were of similar sizes (i.e., at 24, 48, and 72 h AEL). The results indicate that the inhalation of LP^{WJL} volatile does not affect larval feeding behavior, at least during periods when VSF-exposed and non-exposed larvae are of similar size (Fig. 1c).

Recently, it was reported that microbiome-emitted scents influence social behavior, such as mate choice or nestmate recognition[15–18]. Because different scent molecules are readily sensed by olfactory receptors (ORs) in OR-neurons (ORNs)[19–21], we investigated whether ORNs mediated LP^{WJL}-induced host growth. *Drosophila* larvae have 21 ORNs, each expressing a unique OR complex composed of one to two odor-specific ORs and a single universal OR co-receptor (ORCO)[19,22]. When well-known smell-blind $ORCO^{-/-}$ animals[23,24] were subjected to inhalation of LP^{WJL} volatiles, we surprisingly found that the LP^{WJL}-emitted scents still supported their growth (Fig. 1d). The growth rates of $ORCO^{-/-}$ animals were similar to those observed in wild-type or heterozygous $ORCO^{+/-}$ animals (Fig. 1d). These results demonstrate that host growth induced by LP^{WJL}-emitted scents is independent of olfaction, i.e., independent of scent sensing by ORNs.

OR42b is expressed in the gut and its expression is induced by LP^{WJL}-emitted scents

Although it has been believed that the expression of ORs is restricted to the olfactory organ, recent data have revealed that ORs are found outside the olfactory organ in both *Drosophila* and mammals[25,26]. These findings suggest that ectopic ORs have previously unanticipated roles in non-olfactory organs, including the intestine. Based on this, we hypothesized that the microbiome emits VSFs and that enterocytes sense these VSFs via gut-expressing OR. Since stage-specific and tissue-specific expression data suggest that at least twelve ORs are expressed in the larval gut[24,27–30], we assumed that one of these ORs may be the candidate receptor for VSFs in the gut.

To test this hypothesis, we monitored the expression of these ORs in the absence or presence of LP^{WJL} volatiles (Fig. 1e). The result showed that OR42b was greatly upregulated following exposure to LP^{WJL} volatiles (Fig. 1e). Analysis of the intestinal expression of OR42b using reporter flies carrying the OR42b promoter fused to Gal4 (OR42b-Gal4) revealed that OR42b was mainly detected in the enterocytes of the anterior midgut region following inhalation of LP^{WJL} volatiles (Fig. 1f). Additionally, OR42b expression was detected in the boundary region between the proventriculus and midgut, as well as subsets of enteroendocrine cells (EECs) located in the posterior midgut region (Supplementary Fig. 1). Taken together, we conclude that OR42b is expressed in non-olfactory cells, such as enterocytes and EECs, in addition to its known expression in the olfactory organ. Furthermore, intestinal OR42b is induced in response to LP^{WJL}-emitted scents.

Enterocyte OR42b functions as a VSF receptor for growth in an ORCO-independent manner

It is well-known that OR42b is one of the most conserved ORs in many *Drosophila* species[31,32], which suggests that it may play one of the most fundamental functions among ORs. Well-known ligands for OR42b are various chemicals associated with natural *Drosophila* food sources (i.e., microbe-fermented fruits), such as aliphatic esters (e.g., ethyl acetate, ethyl butyrate, and propyl acetate) and 3-hydroxy-2-butanone-associated metabolites (i.e., 3-hydroxy-2-butanone, diacetyl, and 2,3-butanediol)[33,34]. Many *Drosophila* species display attractive behavior toward these chemicals[33–35], suggesting a conserved role of OR42b in ORN during foraging behavior across the *Drosophilidae*. Therefore, we initially thought that some of these attractants act as VSFs. We found that inhalation of one of the aliphatic esters or 3-hydroxy-2-butanone-associated metabolites was sufficient to induce larval growth (Fig. 2a), indicating that known OR42b ligands likely act as VSFs.

Next, we investigated the mechanism by which OR42b acts as a bona fide receptor for VSFs in an ORCO-independent manner. In insects, volatile compounds in scents are normally sensed by a specific OR complexed with a common ORCO, possibly by forming a hetero-tetramer composed of two OR subunits and two ORCO subunits[36]. As OR42b seems to act independently of ORCO (Fig. 1d), we first analyzed whether OR42b forms a functional tetramer in the absence of ORCO. Fluorescence size-exclusion chromatography revealed that GFP-tagged OR42b protein forms a complex corresponding to the size of the tetramer (Fig. 2b). Transmission electron microscopy further

https://doi.org/10.1038/s41467-025-57484-4

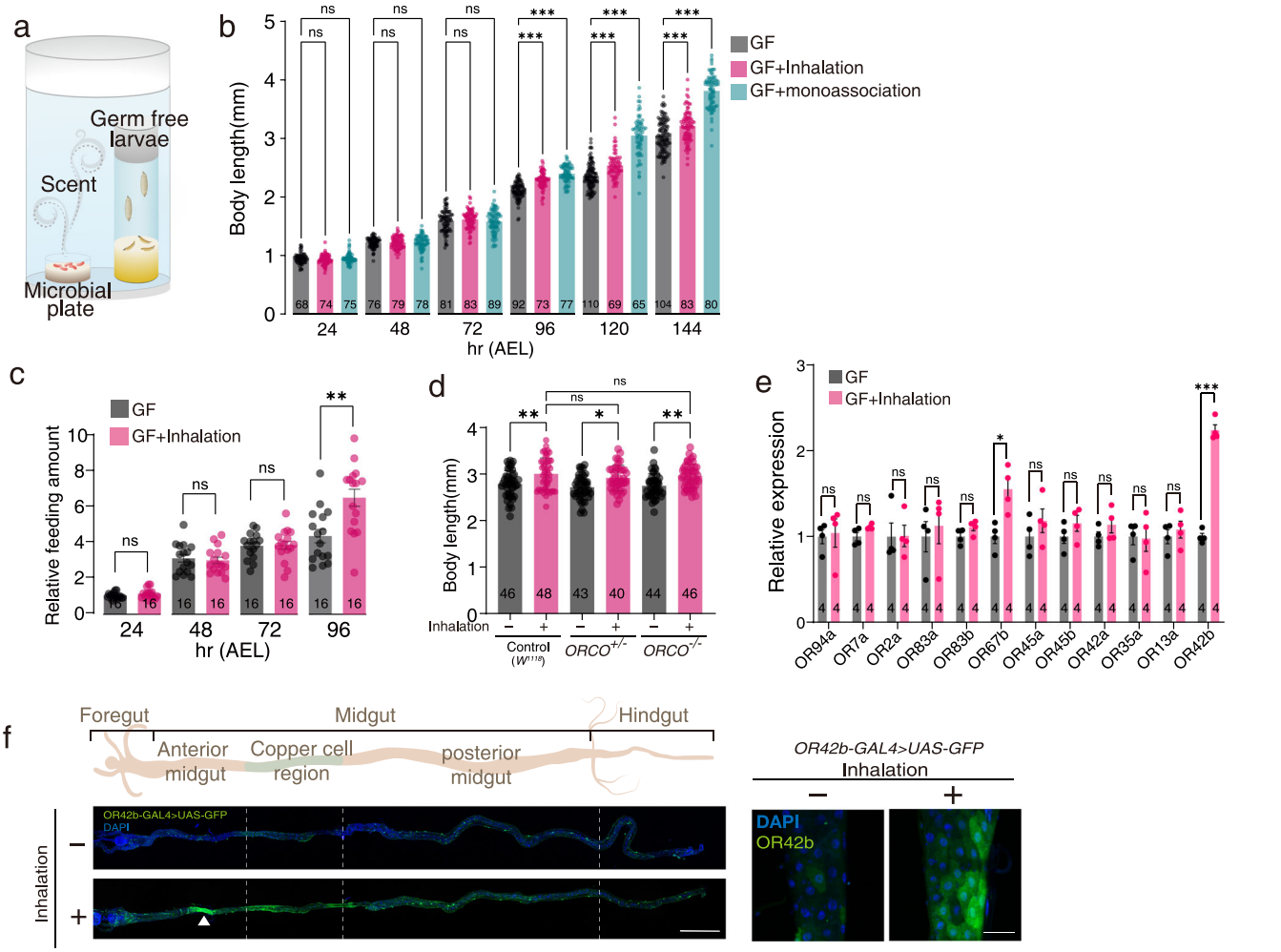

Fig. 1 | Microbiome-emitted scents promote host growth in an olfaction-independent manner. In all cases, germ-free (GF) embryos were treated either without (−) or with (+) inhalation of LP^{WJL} volatiles during entire larval stages. **a** A schematic diagram of the inhalation experiment involving the treatment with LP^{WJL} volatiles. **b** Body length of control GF, GF animals with inhalation of LP^{WJL} volatiles (GF + Inhalation), and GF animals monoassociated with LP^{WJL} (GF + monoassociation). Larval sizes were measured at various hours after egg laying (AEL). $n = 3$ biologically independent experiments. **c** Relative feeding amounts of control GF (GF) and GF animals with inhalation of LP^{WJL} volatiles (GF + Inhalation). Feeding amounts of control GF animals at 24 h AEL were taken arbitrarily as 1. $n = 3$ biologically independent experiments. **d** Body length at 144 h AEL without or with inhalation of LP^{WJL} volatiles. Control, *ORCO*$^{+/-}$, and *ORCO*$^{-/-}$ animals were used. $n = 3$ biologically independent experiments. **e** Real-time qPCR analysis of different ORs. Target gene expression in the GF animals without inhalation of LP^{WJL} volatiles was taken arbitrarily as 1. $n = 4$ biologically independent experiments. **f** *OR42b* promoter activity in the anterior midgut (indicated by filled arrowhead) of *OR42b-GAL4 > UAS-GFP* flies. Representative confocal images of the whole gut (left) and the fluorescence signals in the enterocytes of the anterior midgut (right) are shown. The gut is arranged from anterior to posterior, moving from top to bottom in the photo (right panel). Nuclei were stained with DAPI in blue. Scale bar, 500 μm (left) and 50 μm (right). Data are mean ± s.e.m. *P* values (*$p < 0.05$, **$p < 0.01$, ***$p < 0.001$, ns not significant) are indicated: one-way ANOVA with Tukey's post hoc test in (**b**); two-way ANOVA with Tukey's multiple comparison test in (**d**); unpaired two-tailed *t*-test in (**c**, **e**). Genotypes, sample sizes, and statistical analyses are shown in Supplementary Data 1. Source data are provided in the Source Data file.

validated the formation of homo-tetrameric complexes of OR42b (Fig. 2c).

Utilizing the structural insight into ligand recognition in insect ORs[37], we could predict the presence of a conical (or funnel-like) cavity for ligand access, created by S2, S3, S4, and S6 helices (Fig. 2d). In this model, we could identify Tyr^{156}, Ser^{158}, and Ser^{159} of OR42b as potentially critical residues for ligand binding (Fig. 2d). Accordingly, we generated a UAS fly line carrying a ligand-binding mutant allele of OR42b that is deficient in ligand binding (in which three critical amino acids mutated to Leu^{156}, Ala^{158}, and Ala^{159} residues). Overexpression of this ligand-binding mutant allele by using enterocyte-specific Gal4 driver was sufficient to abolish VSF-induced larval growth, showing that a ligand-binding mutant allele of OR42b acts as a dominant-negative (DN) mutant allele of OR42b (OR42b^{DN}) in the gut (Fig. 2e). These results indicate that critical residues for ligand binding within OR42b are required for VSF-induced growth.

To further validate the role of OR42b in growth and olfaction, we generated an OR42b^{DN} knock-in animal. We observed that VSF-induced larval growth was abolished only in OR42b^{DN} knock-in animals, but not in *ORCO*$^{-/-}$ animals (Fig. 2f). These results indicate that VSF sensing in the gut for growth is likely OR42b-dependent but ORCO-independent.

LP^{WJL} volatiles induce *Btl* signaling activation for gut-associated tracheal branching formation

During the dissection of the gut of *OR42b-Gal4 > UAS-GFP* flies, we routinely observed that OR42b-expressing enterocytes in the anterior midgut are in contact with gut-associated trachea that also express OR42b (Fig. 3a). The tracheal airway, composed of a branched tubular epithelial network throughout the body, acts as a respiratory organ for

https://doi.org/10.1038/s41467-025-57484-4

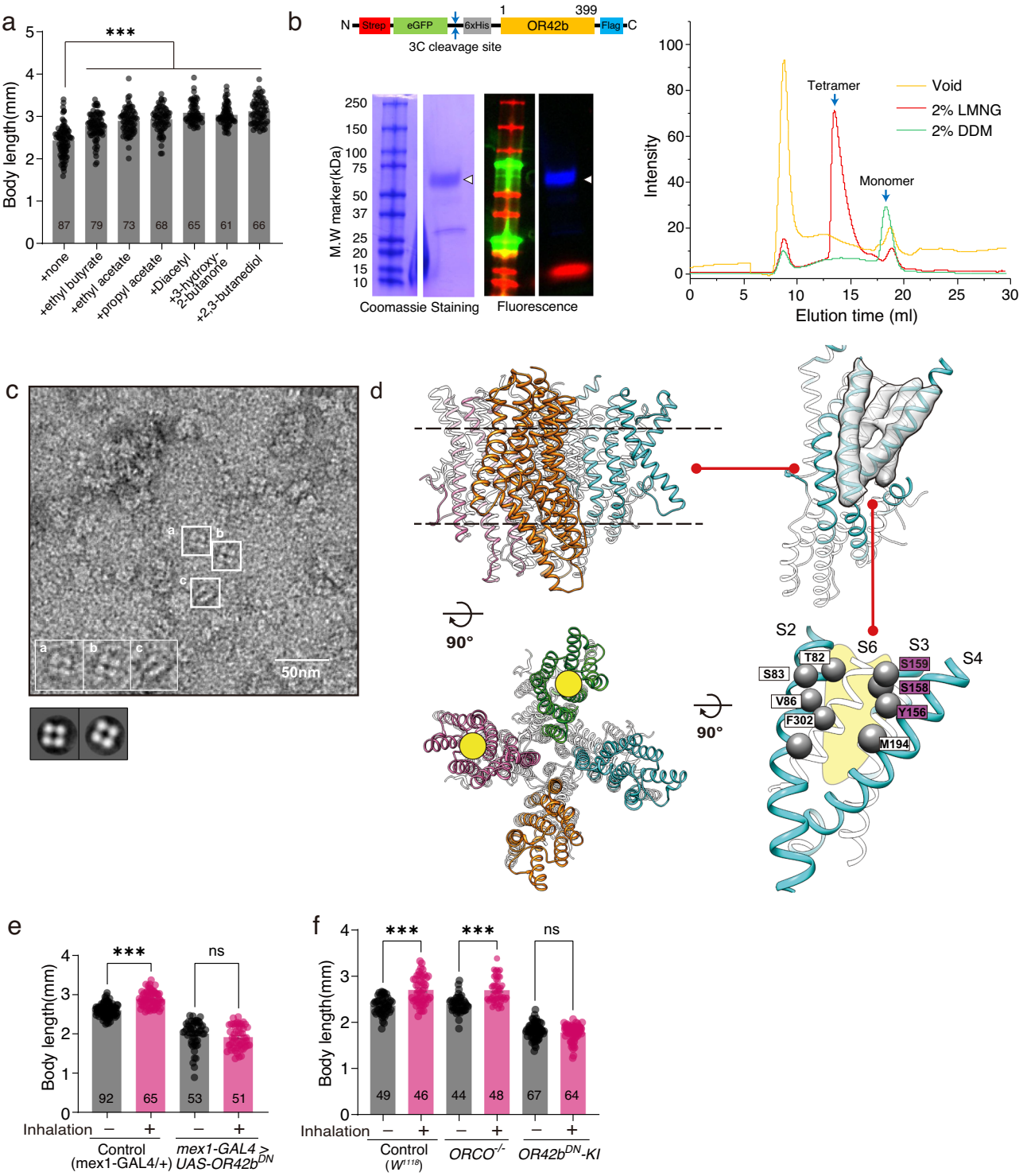

Fig. 2 | OR42b mediates LP^{WJL} volatile-induced host growth in an ORCO-independent manner. a GF embryos were treated either without (+none) or with inhalation of 0.03% (v/v) volatile chemicals (+chemical) during entire larval stages. Larval sizes were measured at 144 h AEL. $n = 3$ biologically independent experiments. **b**, **c** Tetrameric assembly of OR42b. OR42b construct design for expression (**b**, left top) and SDS-PAGE of purified OR42b eluted from affinity chromatography (**b**, left bottom). GFP-OR42b fusion protein is indicated with white arrowheads. Fluorescence size-exclusion chromatography screening under LMNG and DDM detergent conditions (**b**, right). Representative micrograph of OR42b based on negative-stained electron microscopy (**c**). Notable particles are indicated by white boxes, and enlarged (**c**, top). 2D class averages are shown at the bottom right (**c**, bottom). **d** AlphaFold-predicted model of tetrameric OR42b is presented as side and top views. The putative odorant-binding pocket formed by S2, S3, S4, and S6 helices has a conical shape. Conserved residues in the binding pocket are highlighted as gray spheres and Y^{156}, S^{158}, and S^{159} are shown in magenta. **e**, **f** GF embryos were treated either without (−) or with (+) inhalation of LP^{WJL} volatiles during entire larval stages. Larval sizes were measured at 144 h AEL. GF control animals (Control) and GF animals with gut-specific OR42b^{DN} (*Mex1-Gal4 > UAS-OR42b^{DN}*) were used in (**e**); GF Control animals (Control), GF ORCO mutant animals (*ORCO$^{-/-}$*) and GF OR42b^{DN} knock-in animals (*OR42b^{DN}-KI*) were used in (**f**). $n = 3$ biologically independent experiments in (**e**, **f**). Data are mean ± s.e.m. *P* values (***$p < 0.001$, ns not significant) are indicated: one-way ANOVA with Tukey's post hoc test in (**a**); unpaired two-tailed *t*-test in (**e**, **f**). Genotypes, sample sizes, and statistical analyses are shown in Supplementary Data 1. Source data are provided in the Source Data file.

https://doi.org/10.1038/s41467-025-57484-4

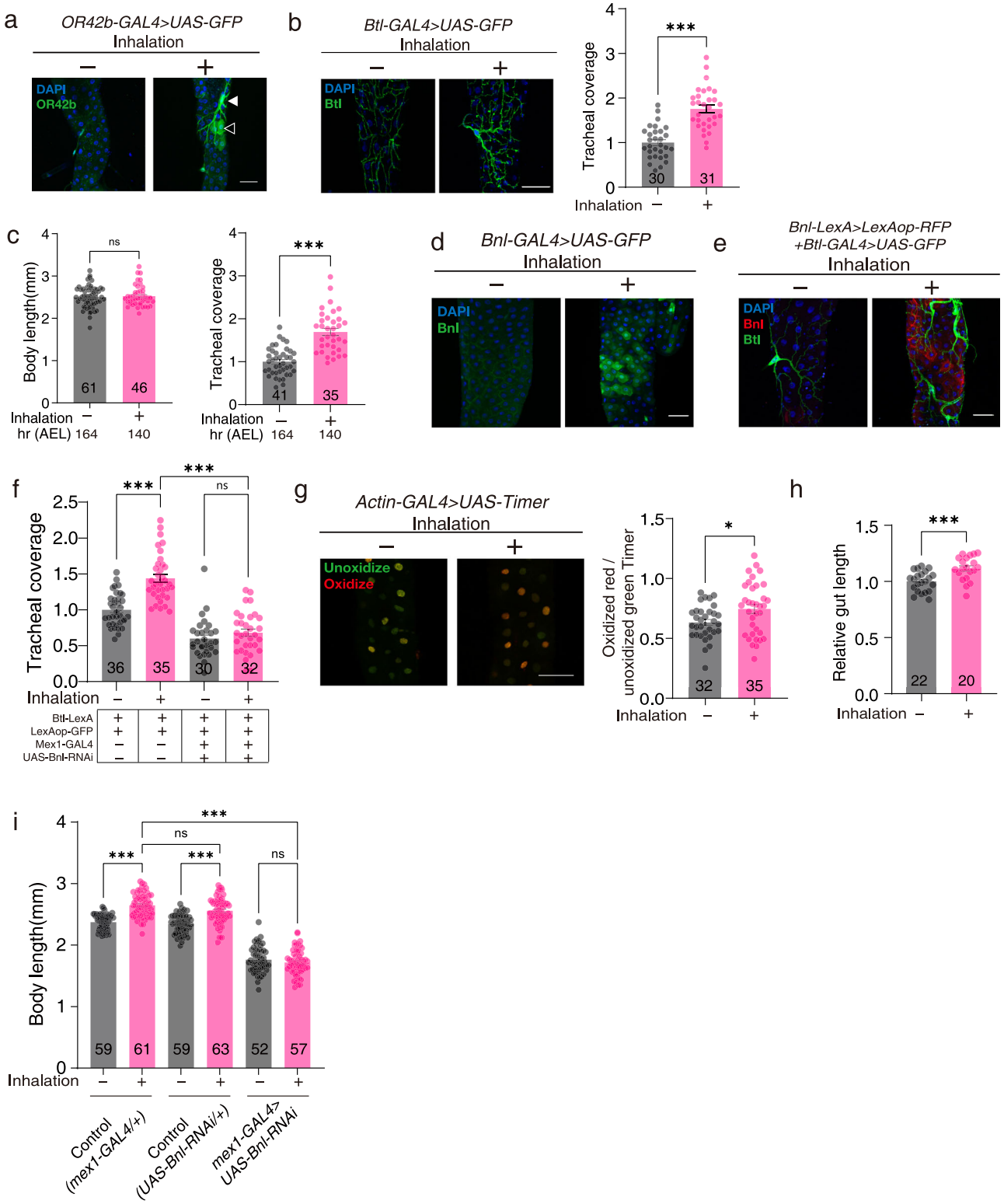

the passage of gas molecules, such as oxygen, to reach internal tissues[38,39]. Tracheal epithelial cells express Breathless (Btl, a homolog of the mammalian FGF receptor) and Btl signaling activation induces tracheal branching formation[40,41]. Btl signaling activation also induces *Btl* expression, thus forming a positive feedback loop[40,42], so we investigated tracheal Btl signaling activation status in the OR42b-expressing gut-associated trachea by examining *Btl* expression patterns. The results showed that LP^{WJL} volatiles strongly activated tracheal Btl signaling, as evidenced by the upregulation of *Btl* expression, and subsequent tracheal branching formation (Fig. 3b). In the absence of LP^{WJL} volatiles, we observed only basal *Btl* expression and reduced branching formation (Fig. 3b).

As LP^{WJL} volatiles promote larval growth, the VSF-exposed larvae are bigger than the non-exposed larvae at the same age (Fig. 1b). To confirm that enhanced tracheal *Btl* expression in the VSF-exposed larvae is not solely due to their larger size, we compared VSF-exposed larvae and non-exposed larvae of similar size (i.e., VSF-exposed larvae at 140 h AEL versus non-exposed larvae at 164 h AEL). The results

Fig. 3 | LP^{WJL} volatiles Promote tracheal branching formation, gut oxygenation, and gut growth. Germ-free embryos were exposed to LP^{WJL} volatiles throughout larval stages (+) or left untreated (−). Third-instar GF larvae were used. **a** *OR42b* expression in the enterocytes (open arrowhead) and gut-associated trachea (filled arrowhead) was observed. **b** LP^{WJL} volatiles enhanced tracheal Btl signaling activation (left: representative image; right: tracheal coverage normalized to untreated larvae, set to 1). $n = 3$ biologically independent experiments. **c** Btl signaling activation is dependent on exposure to LP^{WJL} volatiles. Larvae carrying *Btl-Gal4 > UAS-GFP* were used. To exclude the effect of larval size on tracheal Btl signaling activation, volatile-exposed larvae and non-exposed larvae of similar size were used (left). Relative tracheal coverage of these animals is shown (right). The tracheal coverage of untreated animals was taken arbitrarily as 1. $n = 3$ biologically independent experiments. LP^{WJL} volatiles induced enterocyte *Bnl* expression (**d**) and tracheal *Btl* expression (**e**). **f** Gut-specific *Bnl* knockdown reduced tracheal branching formation. Relative tracheal coverage was shown and the tracheal coverage of untreated control animals was taken arbitrarily as 1. $n = 4$ biologically independent experiments. **g** LP^{WJL} volatiles increased gut oxygenation, measured using Timer, a fluorescence-based oxygen reporter (left: merged oxidized red/unoxidized green Timer image; right: oxidized red/unoxidized green ratio). $n = 4$ biologically independent experiments. **h** The gut lengths, from proventriculus to hindgut, of untreated larvae at 144 h AEL were taken arbitrarily as 1. $n = 3$ biologically independent experiments. **i** Gut-specific *Bnl* knockdown abolishes VSF-induced GF larval growth at 144 h AEL. $n = 3$ biologically independent experiments. Data are mean ± s.e.m., with P values ($^*p < 0.05$, $^{***}p < 0.001$, ns not significant) from unpaired two-tailed t-test (**b**, **c**, **g**, **h**) or two-way ANOVA with Tukey's multiple comparison test (**f**, **i**). The gut is arranged from anterior to posterior, moving from top to bottom in the photo (**a**, **b**, **d**, **e**, **g**). Nuclei were stained with DAPI (blue). Scale bar, 50 µm. Genotypes, sample sizes, and statistical analyses are shown in Supplementary Data 1. Source data are provided in the Source Data file.

showed that VSF-exposed larvae at 140 h AEL still exhibited higher tracheal branching formation than non-exposed larvae at 164 h AEL (Fig. 3c). These findings suggest that Btl activation for tracheal formation is indeed attributable to the exposure to LP^{WJL} volatiles, rather than differences in larval size or developmental stage.

LP^{WJL} volatiles induce airway-gut axis activation via Bnl/Btl signaling for oxygen-mediated regulation of growth

We next examined the molecular mechanism by which LP^{WJL} volatiles induce tracheal Btl signaling activation. Branchless (Bnl, a homolog of mammalian FGF) acts as a known ligand for Btl for its downstream signaling activation[43]. When we examined *Bnl* expression in the gut in the absence of LP^{WJL} volatiles, we found strong basal expression of *Bnl* in the enterocytes of the copper region (Bnl^{copper}) and weak basal expression in the posterior midgut region (Bnl^{posterior}) (Supplementary Fig. 2). Almost no Bnl expression was observed in the anterior midgut region (Bnl^{anterior}) (Supplementary Fig. 2). However, following LP^{WJL} inhalation, we observed a significant induction of Bnl^{anterior} expression, while the intensity of Bnl^{copper} and Bnl^{posterior} expression remained unchanged (Fig. 3d and Supplementary Fig. 2). The expression of Bnl^{anterior} in this region is not uniform across all cells; weak or no expression is observed in some cell populations (Fig. 3d and Supplementary Fig. 2). These results indicate that Bnl^{copper} and Bnl^{posterior} expression are constitutive, while Bnl^{anterior} expression is inducible in the same anterior midgut region where OR42b is inducible. Double labeling of *Bnl* and *Btl* expression confirmed that both *Bnl* expression in the enterocytes and *Btl* expression in the tracheal cells were enhanced following the exposure to LP^{WJL} volatiles (Fig. 3e). Downregulation of *Bnl* expression in the enterocytes decreased both basal and LP^{WJL}-induced tracheal branching formation (Fig. 3f), indicating that LP^{WJL}-induced Bnl in enterocytes is required for tracheal branching formation. Furthermore, we found that gut oxygen concentration and gut size increased following the exposure to LP^{WJL} volatiles (Fig. 3g, h). Furthermore, we found that downregulation of *Bnl* expression in the enterocytes abolished the growth-promoting effect of LP^{WJL} volatiles (Fig. 3i). Taken together, these results indicate that LP^{WJL} volatiles induce airway-gut axis activation via Bnl/Btl signaling for oxygen regulation in organs, which facilitates body growth.

LP^{WJL} volatiles promote DILP2 secretion from the brain for systemic growth control

Previous studies have demonstrated a close relationship between tracheal branching and insulin/IGF signaling pathways[44–46]. This insulin/IGF regulates host homeostatic programs controlling developmental rate as well as organ and body size[11,12,47–49]. To determine whether insulin/IGF mediated LP^{WJL} volatile-dependent growth promotion, we first measured the level of circulating insulin/IGF in the insect blood-like hemolymph. Three insulin/IGFs [referred to as *Drosophila* insulin-like peptides (DILPs) such as DILP2, DILP3, and DILP5] are the major DILPs secreted from insulin/IGF-producing cells (IPCs) of the brain[49,50]. Although the measurement of the circulating levels of growth hormone is indispensable to understand the physiological context, methods to measure endogenous insulin/IGFs levels in the hemolymph have yet to be established in *Drosophila*. To measure the circulating levels of each DILP, we generated double epitope-tagged DILP2, DILP3, or DILP5 knock-in animals (Fig. 4a). Enzyme-linked immunosorbent assay showed that DILP2 is the major form of circulating DILP in larvae, representing ~90% of the IPC-secreted DILPs (Fig. 4a). Further, we found that the circulating level of DILP2, but not DILP3 or DILP5, was significantly augmented following the exposure to LP^{WJL} volatiles (Fig. 4a). The IPC-specific DILP2 knockdown was sufficient to abolish LP^{WJL} volatile-induced animal growth (Fig. 4b). Taken together, these results indicate that LP^{WJL} volatiles promote the release of DILP2 from IPC to hemolymph for systemic growth control.

LP^{WJL} volatiles induce enteroendocrine AstA and CCHA2 peptide hormone expression for brain DILP2 secretion

The molecular mechanism by which LP^{WJL} volatiles can perform long-distance communications with the brain IPC was the focus of our next investigation. Based on our previous observation that gut cells sense the external environment and communicate with the brain via gut hormones[5], we hypothesized that enteric hormones that directly respond to LP^{WJL} volatiles may be involved in communication with IPC in the brain. To test this hypothesis, we monitored the expression of gut hormones altered by LP^{WJL} volatiles (Fig. 4c). We found that two gut peptide hormones, allatostatin-A (AstA) and CCHAmide-2 (CCHA2), were significantly upregulated in a subset of EECs by LP^{WJL} volatiles (Fig. 4c–e). We next analyzed the epistatic relationship between AstA and CCHA2 by using *AstA*$^{-/-}$ and *CCHA2*$^{-/-}$ animals. We found that LP^{WJL} volatile-induced AstA$^+$ EECs were observed in *CCHA2*$^{-/-}$ animals (Fig. 4d), whereas LP^{WJL} volatile-induced CCHA2$^+$ EECs were abolished in *AstA*$^{-/-}$ animals (Fig. 4e and Supplementary Fig. 3). In this condition, we found that the number of EECs does not increase significantly following inhalation of LP^{WJL} (Supplementary Fig. 4). These data indicate that LP^{WJL} volatiles do not affect the total number of EECs, but they do increase the proportion of EECs that secrete AstA or CCHA2. These data also indicate that AstA is required for the inducibility of CCHA2 following the exposure to LP^{WJL} volatiles. Importantly, *OR42b* is expressed specifically in AstA$^+$ EECs (Fig. 4f). Furthermore, we found that AstA receptor-2 (AstAR2) was colocalized with CCHA2 (Fig. 4g) and that AstAR2 was required for VSF-induced *CCHA2* expression (Fig. 4h and Supplementary Fig. 3). Taken together, we concluded that LP^{WJL} volatiles induce *AstA* expression in *OR42b*-expressing EECs that in turn induces *CCHA2* expression in *AstAR2*-expressing EECs.

AstA and CCHA2 are found to be expressed in diverse cells, such as fat body cells and EECs, and are known to affect various aspects of host physiology, at least partially by modulating IPCs[51–53]. Therefore, we determine whether LP^{WJL} volatile-induced AstA and CCHA2

https://doi.org/10.1038/s41467-025-57484-4

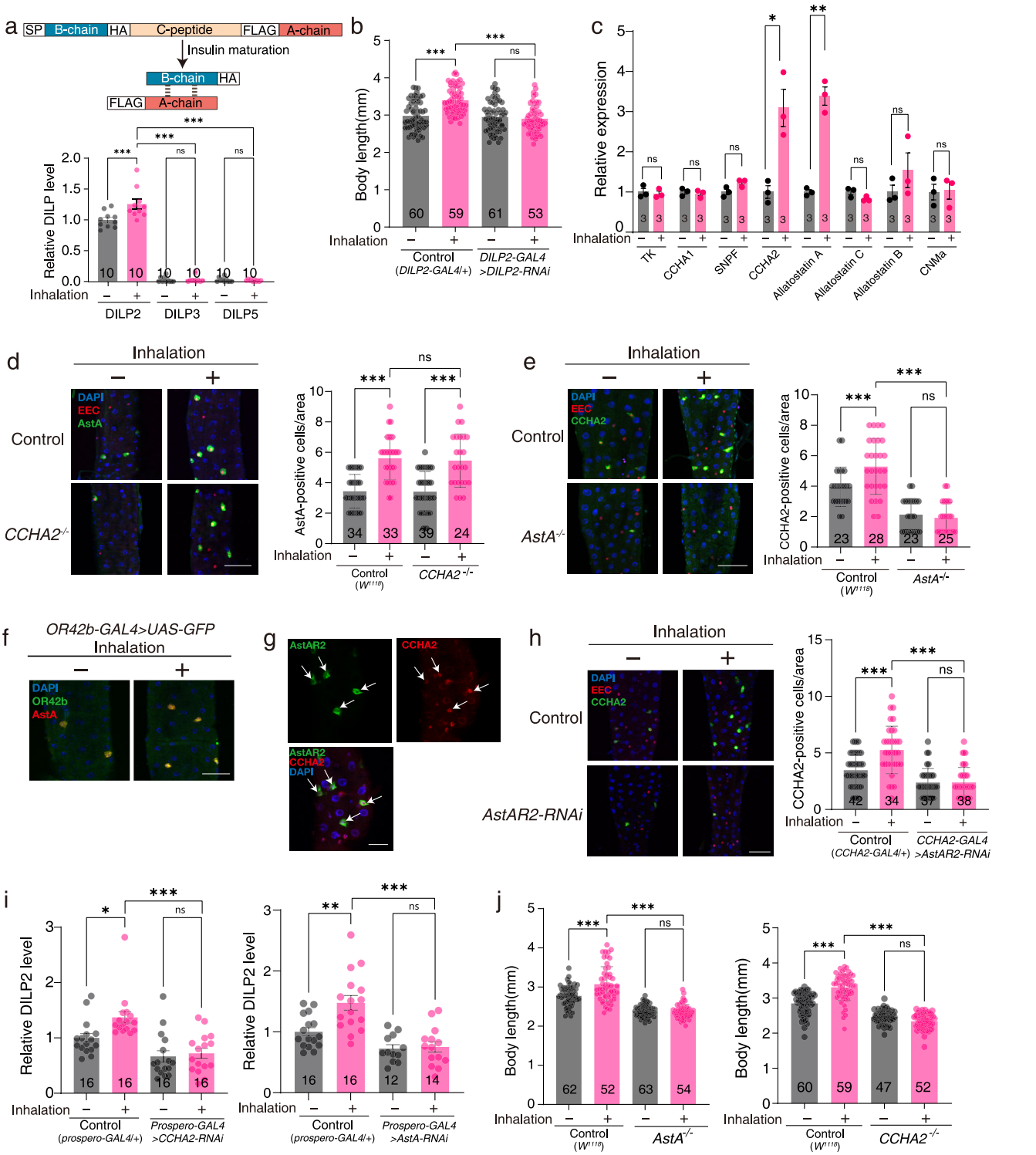

mediated DILP2 secretion. For this, we first analyzed the circulating DILP2 levels following EEC-specific knockdown of *AstA* or *CCHA2* expression by using Prospero-Gal4. The results showed that the knockdown of intestinal *AstA* or *CCHA2* abrogated LP^{WJL} volatile-induced DILP2 secretion (Fig. 4i). Consistent with these hormone knockdown data, we found that mutation of one of these hormones was sufficient to abolish LP^{WJL} volatile-induced body growth (Fig. 4j), indicating that both hormones were required for body growth. Taken together, these data indicate that LP^{WJL} volatile-induced intestinal AstA and CCHA2 hormones are required for DILP2 secretion from brain IPC, thereby forming the somatotrophic gut-brain axis.

LP^{WJL} volatiles inactivate the Hippo pathway leading to Yorkie nuclear localization

We investigated the intracellular signaling pathway by which OR42b mediates VSF-responsive gene expression. Because Yorkie, a transcriptional coactivator of the Hippo pathway, is shown to be required for *Bnl* expression[54], we first analyzed whether the Hippo pathway acted downstream of OR42b for the expression of VSF-responsive genes. In the absence of growth signaling during which the Hippo pathway is constitutively activated, Merlin, in association with Kibra and Expanded, forms a membrane-associated complex for sequential activation of two downstream kinases, Hippo and

Fig. 4 | LP^{WJL} volatiles induce gut-brain somatotrophic axis for systemic growth. Germ-free embryos were treated without (−) or with (+) inhalation of LP^{WJL} volatiles during larval stages. Larvae at 144 h AEL were analyzed. **a** Schematic of HA/FLAG epitope-tagged DILP2, 3, or 5 knock-in strategy (top) and hemolymph DILP level (bottom) in GF knock-in animals. DILP2 levels of DILP2 knock-in animals without LP^{WJL} volatiles were set as 1. $n = 3$ biologically independent experiments. **b** Body length of GF control and GF DILP2-RNAi larvae. $n = 3$ biologically independent experiments. **c** Real-time qPCR analysis of gut hormone expression in the GF animals. Control values without LP^{WJL} volatiles were set as 1. $n = 3$ biologically independent experiments. **d** AstA$^+$ EEC numbers in GF control and GF *CCHA2*$^{-/-}$ animals. $n = 3$ biologically independent experiments. **e** CCHA2$^+$ EEC numbers in GF control and GF *AstA*$^{-/-}$ animals. $n = 3$ biologically independent experiments. **f** Colocalization of AstA$^+$ EEC with OR42b. Colocalization of AstA receptor 2 (AstAR2) with CCHA2$^+$ EECs (**g**); and CCHA2$^+$ EEC numbers in GF control and GF *AstAR2-RNAi* animals (**h** left, representative image; **h** right, CCHA2$^+$ EEC number/gut). $n = 3$ biologically independent experiments. **i** Relative levels of hemolymph DILP2 in GF control, GF *CCHA2-RNAi*, and GF *AstA-RNAi*. DILP2 levels of GF control (DILP2 knock-in) animals without LP^{WJL} volatiles were set as 1. $n = 3$ biologically independent experiments. **j** Body length of GF control, GF *AstA*$^{-/-}$, and GF *CCHA2*$^{-/-}$ animals. $n = 3$ biologically independent experiments. Gut samples were taken from a 0.1 mm^2 region to count AstA$^+$ or CCHA2$^+$ cells (d,e, and h). Data are mean ± s.e.m., with *P* values (*$p < 0.05$, **$p < 0.01$, ***$p < 0.001$, ns not significant); unpaired two-tailed *t*-test in (**c**); two-way ANOVA with Tukey's multiple comparison test in (**a**, **b**, **d**, **e**, **h**–**j**). The gut is arranged from anterior to posterior, moving from top to bottom in the photo (**d**–**h**). Nuclei were stained with DAPI (blue). Scale bar, 50 µm. Genotypes, sample sizes, and statistical analyses are shown in Supplementary Data 1. Source data are provided in the Source Data file.

Warts[55,56]. Activated Warts inhibit Yorkie nuclear localization by phosphorylating Yorkie[57]. To assess the subcellular localization of endogenously expressed OR42b, we generated OR42b-FLAG knock-in animals containing C-terminal FLAG epitope-tagged OR42b. By combining OR42b-FLAG knock-in flies with Merlin-YFP flies, we assessed the subcellular localization of Merlin-YFP and OR42b-FLAG before and after the exposure to LP^{WJL} volatiles. The result showed that Merlin and OR42b were colocalized in the membrane under basal conditions (Fig. 5a). Importantly, we found that both proteins rapidly dispersed from the membrane following the exposure to LP^{WJL} volatiles (Fig. 5a). As membrane localization of the Merlin complex is essential for downstream Hippo pathway activation[55], we speculated that VSF-induced dispersal of the membrane-localized Merlin complex inactivated the Hippo pathway, leading to nuclear localization of Yorkie. To test this possibility, Yorkie localization was analyzed before and after the exposure to LP^{WJL} volatiles. The results showed that cytoplasmic Yorkie rapidly translocated into the nucleus following the exposure to LP^{WJL} volatiles (Fig. 5b), indicating that VSFs, acting as growth factors, inactivated the Hippo pathway leading to Yorkie nuclear localization.

OR42b is required for the regulation of the Hippo pathway

In contrast to VSF-induced dispersal of membrane-localized OR42b (Fig. 5a), LP^{WJL} volatiles do not affect membrane localization of OR42b^{DN}, showing constitutive membrane localization (Fig. 5c). These data indicate that VSF binding to OR42b likely initiated the dispersal of membrane OR42b. Consistently, OR42b^{DN} overexpression in the gut cells led to a constitutive membrane localization of the Merlin complex (Fig. 5d), which prevented Yorkie nuclear translocation (Fig. 5e). These data suggest that the Merlin complex was tethered to the constitutively membrane-localized OR42b^{DN} to activate the Hippo pathway (see also Fig. 5f). To further investigate whether the physical presence of OR42b on the membrane was indeed required for the maintenance of membrane localization of the Merlin complex, the Merlin localization was analyzed under OR42b-knockdown condition. In these OR42b-knockdown animals, we found that membrane localization of the Merlin complex was abolished even in the absence of LP^{WJL} volatiles (Fig. 5d), showing a constitutive nuclear localization of Yorkie (Fig. 5e). These results indicate that the membrane localization status of OR42b controls Merlin complex localization and corresponding Hippo pathway activity (see also Fig. 5f). OR42b-knockdown animals having dispersed Merlin complex showed constitutive Hippo pathway inactivation (i.e., nuclear localization of Yorkie) whereas OR42b^{DN}-overexpressing animals having constitutive membrane localization of Merlin complex showed constitutive Hippo pathway activation (i.e., cytoplasmic localization of Yorkie) (Fig. 5f).

OR42b-modulated Hippo pathway regulates VSF-responsive gene expression

We next analyzed whether the Hippo pathway-modulated Yorkie controls VSFs-responsive gene expression. We found that LP^{WJL} volatiles failed to induce the expression of all VSF-responsive genes (i.e., *Btl*, *Bnl*, and *AstA*) in Yorkie-knockdown animals (Supplementary Fig. 5). In contrast, all VSF-responsive genes displayed high levels of expression even in the absence of LP^{WJL} volatiles in animals expressing the active form of Yorkie (Supplementary Fig. 5). These results indicate that Hippo pathway activity and subsequent Yorkie activity are crucial for VSF-induced target gene expression following the exposure to LP^{WJL} volatiles.

To further validate the role of OR42b in Hippo/Yorkie pathway regulation, we generated OR42b-knockout (*OR42b*$^{-/-}$) animals carrying a null mutant allele of OR42b that lacked all protein-coding sequences. In these *OR42b*$^{-/-}$ animals, we found LP^{WJL} volatile-independent constitutive activation of *Btl* and *AstA* in trachea and EECs, respectively (Fig. 6a, b). Consistent with these data, EEC-specific *OR42b-RNAi* is sufficient to increase the number of AstA$^+$ EECs (Fig. 6b). The constitutive activation of *Btl* and *AstA* observed in *OR42b*$^{-/-}$ animals indicates constitutive activation of Yorkie. Accordingly, *OR42b*$^{-/-}$ animals showed enhanced body growth even in the absence of LP^{WJL} volatiles (Fig. 6c), indicating that the absence of OR42b is responsible for Hippo pathway inactivation (i.e., Yorkie activation). The high *AstA* expression and growth promotion observed in *OR42b*$^{-/-}$ animals were reduced to the level of control flies when OR42b expression was reintroduced in OR42b-expressing tissues. (i.e., *OR42b-Gal4* > *UAS-OR42b* in *OR42b*$^{-/-}$ animals) (Fig. 6d–f). Furthermore, the growth promotion observed in *OR42b*$^{-/-}$ animals was abolished in double mutant animals lacking both *OR42b* and *AstA* (Fig. 6g). These results indicate that the constitutive *AstA* expression and enhanced organ/body growth in the absence of LP^{WJL} volatiles are indeed due to the absence of OR42b, and that AstA is required for the growth promotion observed in *OR42b*$^{-/-}$ animals. In contrast to OR42b$^{-/-}$ animals, LP^{WJL} volatile-induced *Btl*, *Bnl*, and *AstA* expression (Supplementary Fig. 6a, b), and subsequent body growth were completely abolished in OR42b^{DN} knock-in animals (Fig. 2f), indicating that signal-dependent Yorkie activation was abolished. Importantly, inactivation of OR42b in one of three VSF-responsive organs or cells (by overexpressing *OR42b*^{DN} in the trachea, enterocytes, or AstA$^+$ EECs) was sufficient to abolish LP^{WJL} volatile-induced host growth (Supplementary Fig. 6c), indicating that OR42b activation in both airway and gut is required for animal growth. Taken together, we could conclude that LP^{WJL}-emitted VSFs induce OR42b dispersal that in turn induces Hippo pathway inactivation leading to Yorkie activation for growth-promoting gene expression.

https://doi.org/10.1038/s41467-025-57484-4

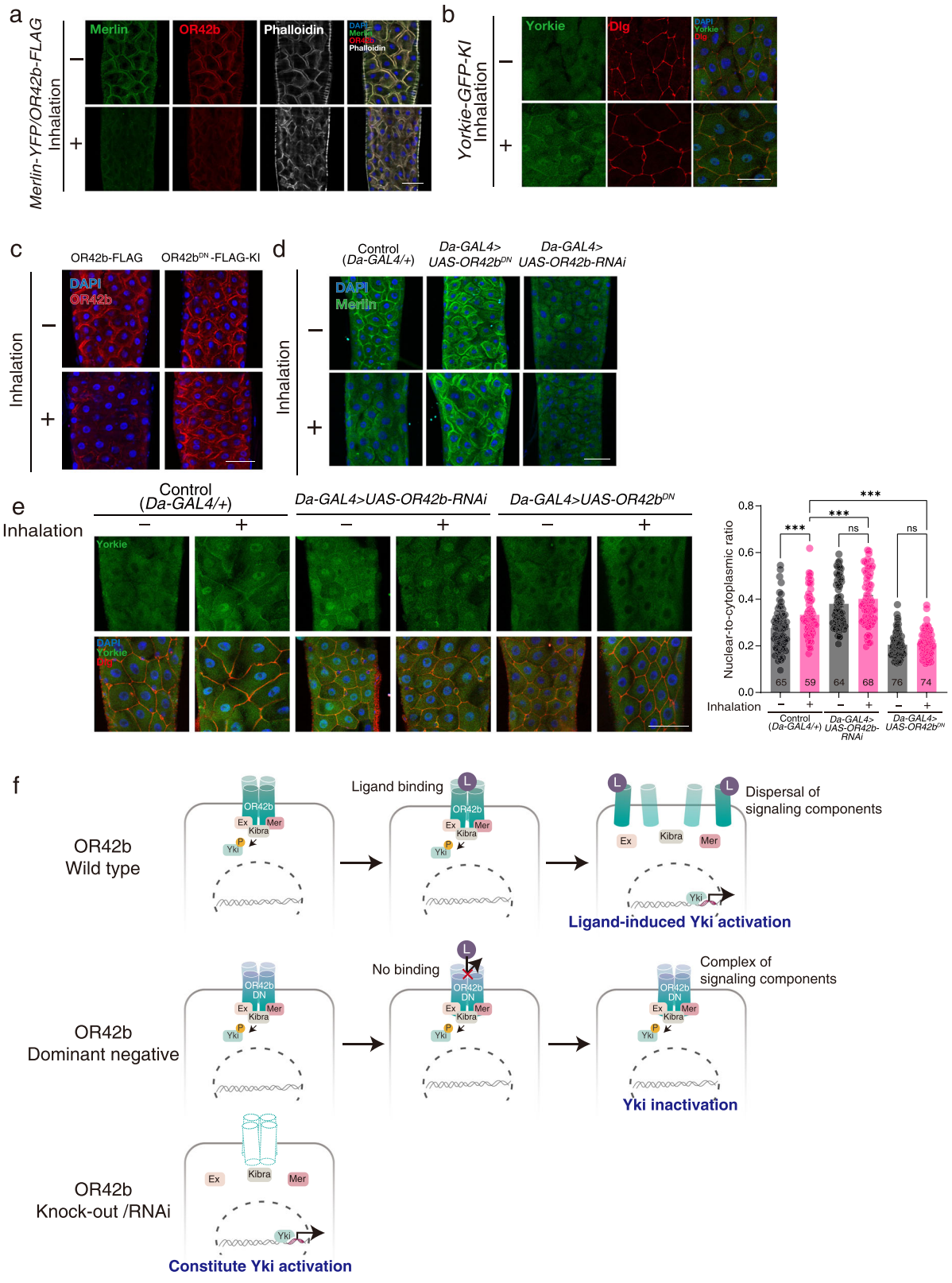

LP^{WJL}-emitted (2R,3R)-2,3-butanediol is responsible for the activation of airway-gut-brain axis for animal growth

We next analyzed whether different OR42b ligands (i.e., aliphatic esters or 3-hydroxy-2-butanone-associated metabolites) capable of inducing larval growth (Fig. 2a) were indeed released from the LP^{WJL}. Metabolic pathway analysis revealed that pyruvate was converted into 3-hydroxy-2-butanone which was subsequently converted into diacetyl and three isomers of 2,3-butanediol (Fig. 7a). Among three 2,3-butanediol stereoisomers, i.e., the R form (2R,3R-butanediol), S form (2S,3S-butanediol), and meso form (2R,3S-butanediol), only (2R,3R)-stereoisomer of 2,3-butanediol induced tracheal cell activation and subsequent host growth promotion (Supplementary Fig. 7a, b). The treatment of (2R,3R)-2,3-butanediol volatiles induced OR42b dispersal in the enterocyte in both wildtype and ORCO

Fig. 5 | LP^{WJL} volatiles modulate the Hippo-Merlin-Yorkie pathway via non-olfactory OR42b. In all cases, germ-free embryos were treated either without (−) or with (+) inhalation of LP^{WJL} volatiles during entire larval stages. Larvae at 144 h AEL were used. **a** Membrane colocalization of Merlin and OR42b in the absence of LP^{WJL} volatiles, and dispersal of membrane Merlin-OR42b following the exposure to LP^{WJL} volatiles. Enterocytes from OR42b-FLAG knock-in animals carrying Merlin-YFP were stained. Phalloidin staining was performed to visualize the brush border membrane of enterocytes. **b** Nuclear Yorkie translocation of enterocytes following the exposure to LP^{WJL} volatiles. Staining of Dlg, a septate junction marker, and DAPI were included to facilitate visualization of the cytoplasmic and nuclear regions of individual cells. **c** LP^{WJL} volatile-independent constitutive membrane localization of OR42b^{DN}. Enterocytes from OR42b^{DN}-FLAG knock-in animals were stained. Membrane localization of Merlin (**d**) and nuclear localization of Yorkie (**e**) in enterocytes from GF *Da-Gal4* control, GF *Da-Gal4 > UAS-OR42b^{DN}*, and GF *Da-Gal4 > UAS-OR42b-RNAi* animals. Nuclear-to-cytoplasmic ratio of Yorkie was shown (**e**). $n = 3$ biologically independent experiments. **f** A model for Hippo/Yorkie pathway in OR42b wildtype, dominant-negative, and RNAi/knockout. Data are mean ± s.e.m. *P* values (***$p < 0.001$, ns not significant) are indicated; two-way ANOVA with Tukey's multiple comparison test in (**e**). The gut is arranged from anterior to posterior, moving from top to bottom in the photo (**a**–**e**). Nuclei were stained with DAPI in blue. Scale bar, 50 μm. Genotypes, sample sizes, and statistical analyses are shown in Supplementary Data 1. Source data are provided in the Source Data file.

mutant backgrounds (Supplementary Fig. 7c), indicating that OR42b can sense (2R,3R)-2,3-butanediol in an ORCO-independent manner. As aliphatic ester production is largely dependent on the presence of precursors (e.g., both ethanol and aliphatic acid) in culture media[58], our precursor-free culture of LP^{WJL} likely favorized the production of 3-hydroxy-2-butanone and its associated metabolites, rather than aliphatic ester production. Gas chromatography–mass spectrometry (GC-MS) analysis of LP^{WJL}-emitted gas revealed that LP^{WJL} indeed emitted 3-hydroxy-2-butanone, diacetyl, and (2R,3R)-2,3-butanediol (Fig. 7b). Quantitative analyses showed that (2R,3R)-2,3-butanediol was the major VSF emitted from LP^{WJL} (Fig. 7b). Consistently, we observed that treatment with (2R,3R)-2,3-butanediol was sufficient to trigger calcium mobilization in the OR42b-expressing cells such as tracheal cells and AstA^{+} EECs (Supplementary Movies 1 and 2). In contrast, the S form or meso form of 2,3-butanediol failed to induce calcium mobilization in the trachea (Supplementary Movies 3 and 4), indicating that the calcium response is specific to (2R,3R)-2,3-butanediol. Computational analysis of (2R,3R)-2,3-butanediol binding to OR42b further revealed two potential binding pockets (Supplementary Fig. 8).

To determine whether LP^{WJL}-emitted (2R,3R)-2,3-butanediol was required for host growth, we generated mutant bacteria incapable of producing (2R,3R)-2,3-butanediol. Toward this end, we deleted the acetolactate synthetase (ALS) gene responsible for α-acetolactate (a precursor molecule for 3-hydroxy-2-butanone) production to generate LP^{WJL}ΔALS. GC-MS analysis confirmed that the LP^{WJL}ΔALS largely lost its ability to produce all three OR42b ligands including (2R,3R)-2,3-butanediol (Fig. 7b). Importantly, in contrast to LP^{WJL} volatiles, LP^{WJL}ΔALS volatiles showed impaired activation of airway-gut-brain axis (including tracheal branching formation, organ oxygenation, gut hormone activation, and DILP2 release) without affecting Hippo pathway (as evidenced by unchanged Merlin membrane localization before and after inhalation), resulting in diminished growth-promoting activity (Fig. 7c–g, and Supplementary Fig. 9). All these defects were reversed by volatiles of LP^{WJL}ΔALS_ALS strain (a genetically-rescued strain by re-introducing ALS gene into the LP^{WJL}ΔALS shown in the Fig. 7b) or volatiles of LP^{WJL}ΔALS together with (2R,3R)-2,3-butanediol (Fig. 7c–g, and Supplementary Fig. 9). These findings demonstrate that commensal LP^{WJL} emitted (2R,3R)-2,3-butanediol as a major VSF, which in turn activated OR42b-dependent airway-gut-brain axis for host developmental homeostasis.

Discussion

Revolutionary discoveries of the role of the microbiome highlight novel and essential aspects of animal physiology. Even extremely complex physiological phenomena, such as individual decision-making and behavior, are also influenced by the microbiome[58,59]. Amazingly, animals, such as honeybees and hyenas, are known to communicate and identify each other via volatile scent molecules emitted from their microbiome, which acts as a sign of hive membership[15,16,60,61]. In this case, the olfactory organ may allow the transmission of olfactory signals to the brain, which aids animal-to-animal communication. In the present study, we identified a previously unrecognized olfaction-independent role of microbiome-emitted scents in animal growth via airborne interactions between host and microbe.

It is generally accepted that ORCO is indispensable for the function of individual ORs in sensing scent molecules by forming heterotetramers[19,22,36]. However, our results revealed that OR42b can function in an ORCO-independent manner (Fig. 1d and Supplementary Fig. 7c). Recent genome sequencing data revealed that a single ORCO gene is present in the genome of all insect orders except *Archaeognatha*, an evolutionarily primitive insect order such as the jumping bristletail (*Machilis hrabei*)[36,62]. Interestingly, *Machilis hrabei* OR5 (MhOR5) formed homotetramers[37], suggesting that, prior to the emergence of ORCO, the ancestral OR is able to be functional without the assistance of ORCO. Our study suggests the presence of an OR42b homotetramer (Fig. 2b, c), with structural resemblance to MhOR5 (Supplementary Fig. 8). Notably, both OR42b and MhOR5 share similarities in the bulky hydrophobic residues located at the interfaces between subunits (Supplementary Fig. 8). These findings collectively support the idea that OR42b has the potential to form a homotetramer independent of ORCO. Based on these data, it can be speculated that the olfaction-independent non-neuronal OR function (e.g., ORCO-independent intestinal and airway OR42b function) may be phylogenetically primitive, which predates olfaction-dependent and ORCO-dependent OR function. In this context, it is not surprising that OR expression is not restricted to ORNs, from *Drosophila* to humans, but occurs in various non-olfactory organs including the gut. However, the in vivo biological functions of ORs expressed in non-olfactory organs remain largely unknown. The present study presents an extraordinary case of non-olfactory OR function transducing the microbiome signal contributing to essential host physiology, such as growth (Fig. 8).

What are the advantages of air-diffusible growth factors? We found that (2R,3R)-2,3-butanediol can serve as a potent attractant for both *Drosophila* larvae and adults (Supplementary Fig. 10). We also found that the sensing of (2R,3R)-2,3-butanediol by the olfactory organ is dependent on both OR42b and ORCO (Supplementary Fig. 10). Consistent with these data, we found that *Drosophila* showed a stronger attraction to LP^{WJL} compared to LP^{WJL}ΔALS, and this attraction is also dependent on both OR42b and ORCO (Supplementary Fig. 10). Based on these findings, it is tempting to speculate that the airborne nature of bacterial (2R,3R)-2,3-butanediol enables it to function as an attractant, thereby increasing the chance of encountering *Drosophila* in their natural habitat and consequently enhancing the probability of colonization in the *Drosophila* gut. Indeed, *Lactiplantibacillus* is one of the primary members of gut commensal bacteria found in both laboratory-reared and wild-caught *Drosophila*[12]. Once introduced into the gut, (2R,3R)-2,3-butanediol acts as a growth-promoting factor in an OR42b-dependent but ORCO-independent manner. These data indicate that bacterial (2R,3R)-2,3-butanediol serves a dual role as both an attractant and a growth-promoting factor for *Drosophila*,

https://doi.org/10.1038/s41467-025-57484-4

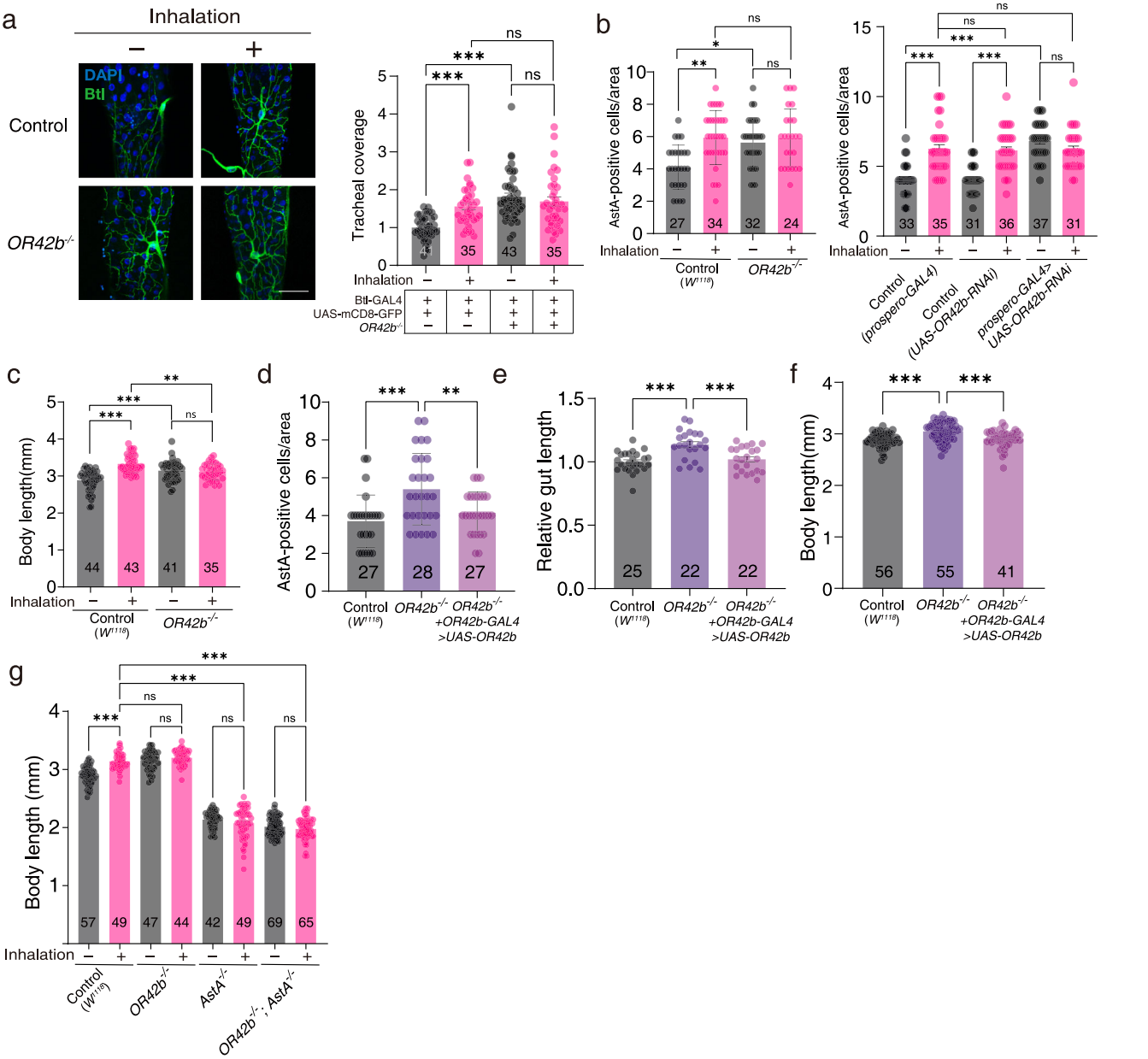

Fig. 6 | *OR42b*$^{-/-}$ animals showed constitutive Yorkie activation and enhanced body growth even in the absence of LP^{WJL} volatiles. In all cases, germ-free embryos were treated either without (−) or with (+) inhalation of LP^{WJL} volatiles during entire larval stages. Larvae at 144 h AEL were used. **a** *Btl* expression (left) and relative tracheal coverage (right) in GF control and GF *OR42b*$^{-/-}$ animals. The tracheal coverage of untreated GF control animals was taken arbitrarily as 1. The gut is arranged from anterior to posterior, moving from top to bottom in the photo. $n = 3$ biologically independent experiments. **b** Quantitative analysis of AstA^{+} EEC number per gut in GF control and GF *OR42b*$^{-/-}$ animals (left) or GF *OR42b-RNAi* animals (right). $n = 3$ biologically independent experiments. **c** Body length in GF control and GF OR42b$^{-/-}$ animals. $n = 3$ biologically independent experiments. Genetic rescue experiment by expressing *OR42b* in the OR42b knock-out animal. AstA^{+} EEC number per gut (**d**), and growth promotion of gut (**e**) and body (**f**) were measured. $n = 3$ biologically independent experiments in (**d**–**f**). Gut sizes of control GF animals were taken arbitrarily as 1 (**g**). $n = 3$ biologically independent experiments. Body length in GF control, GF *OR42b*$^{-/-}$, GF *AstA*$^{-/-}$, and GF *OR42b*$^{-/-}$*; AstA*$^{-/-}$ animals. In each gut sample, an area (0.1 mm^2) of a microscopic image from a similar gut region was randomly selected to count the number of AstA^{+} cells (**b**, **d**). Data are mean ± s.e.m. *P* values (*$p < 0.05$, **$p < 0.01$, ***$p < 0.001$, ns not significant) are indicated; one-way ANOVA with Tukey's post hoc test in (**d**–**f**); two-way ANOVA with Tukey's multiple comparison test in (**a**–**c**, **g**). Nuclei were stained with DAPI in blue. Scale bar, 50 µm. Genotypes, sample sizes, and statistical analyses are shown in Supplementary Data 1. Source data are provided in the Source Data file.

illustrating a striking example of airborne mutualism between host and microbe.

Considering millions of years of co-evolution between microbiome and host, the mutual benefit in the form of growth stimulation likely represents one of the oldest forms of host-microbiome mutualism. Currently, two commensal members of *Drosophila*, *Lactiplantibacillus*, and *Acetobacter*, are the best-known growth-promoting microorganisms[11,12,63]. It has been shown that D-alanine esterification on teichoic acids contributes to *Lactiplantibacillus*-mediated *Drosophila* larval growth promotion under conditions of chronic undernutrition[64]. In this study, the LP NC8 wild-type strain (NC8^{WT}) was used as a growth-promoting strain. It was found that mutant bacteria lacking the dlt operon (NC8$^{\Delta dlt}$), which results in the loss of D-alanine esterification on teichoic acids, showed a significant growth delay when colonizing GF animals. In contrast to this result, our preliminary results showed that both NC8^{WT} and NC8$^{\Delta dlt}$ exhibited growth-

https://doi.org/10.1038/s41467-025-57484-4

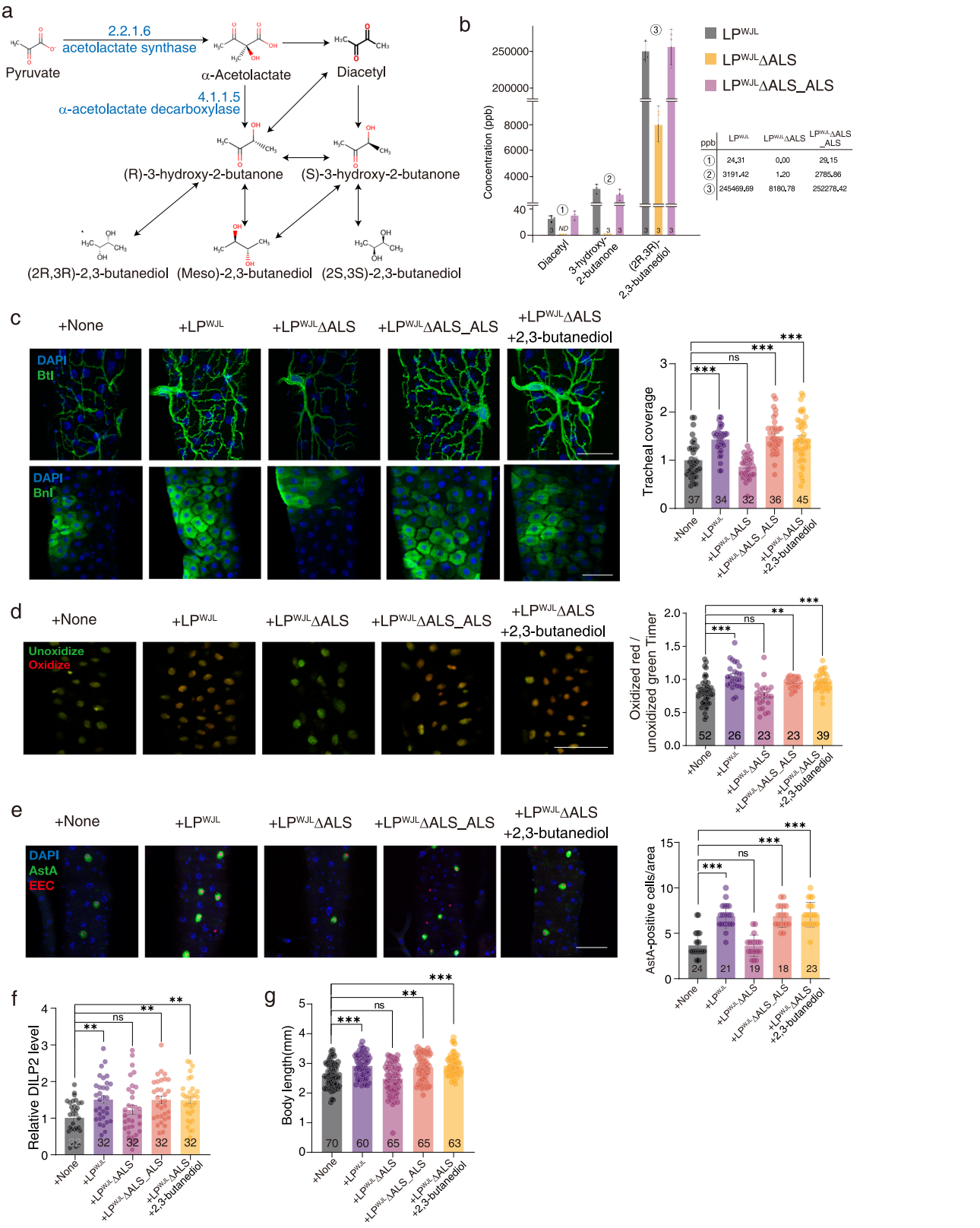

promoting activity under our experimental inhalation conditions (Supplementary Fig. 11), indicating that the dlt operon is not involved in VSF-mediated growth promotion. Consistent with this idea, the NC8$^{\Delta ALS}$ and NC8$^{\Delta dlt_\Delta ALS}$ strains—(2R,3R)-2,3-butanediol-deficient mutant counterparts of NC8^{WT} and NC8$^{\Delta dlt}$, respectively—created by deleting the ALS gene, showed impaired inhalation-dependent larval growth (Supplementary Fig. 11). These findings suggest that LP strains promote host growth in *Drosophila* through at least two independent mechanisms: dlt operon-mediated D-alanine esterification on teichoic acids and ALS-mediated production of (2R,3R)-2,3-butanediol.

In the case of *Acetobacter*, metabolic pathway analyses reveal that a growth-promoting strain of *Acetobacter*, previously isolated from the *Drosophila* gut[11], is unable to synthesize (2R,3R)-2,3-butanediol (Supplementary Fig. 12). However, our preliminary

Fig. 7 | LP^{WJL}-emitted (2R,3R)-2,3-butanediol is responsible for the activation of the airway-gut-brain axis during animal growth. a A biosynthetic pathway of 2,3-butanediol production from pyruvate. **b** GC-MS for quantitative analysis of different metabolites emitted by LP^{WJL}, LP^{WJL}ΔALS, and LP^{WJL}ΔALS_ALS strains. $n = 3$ biologically independent experiments. Representative image of *Btl* and *Bnl* expression in trachea and enterocytes, respectively (**c**, left), relative tracheal coverage (**c**, right), representative merged image of oxidized red and unoxidized green Timer in enterocytes (**d**, left), ratio of oxidized red to unoxidized green Timer (**d**, right), representative image of *AstA* expression in EECs (**e**, left), quantitative analysis of AstA$^+$ EEC number (**e**, right), quantitative analysis of circulating DILP2 level (**f**), and body length (**g**) were analyzed. $n = 3$ biologically independent experiments in (**c**–**g**). Relative values of GF control animals without inhalation of LP^{WJL} volatiles were taken arbitrarily as 1 (**c**, **f**). In all cases, GF embryos were treated either without (+none) or with inhalation of volatiles from LP^{WJL} (+LP^{WJL}) bacteria, LP^{WJL} ΔALS (+LP^{WJL} ΔALS) bacteria, or LP^{WJL}ΔALS_ALS (+LP^{WJL}ΔALS_ALS) bacteria during entire larval stages. In the case of co-stimulation, GF embryos were treated with inhalation of volatiles from both LP^{WJL} ΔALS bacteria and (2R,3R)-2,3-butanediol (0.3% v/v) (+LP^{WJL} ΔALS+2,3-butanediol). Larvae at 144 h AEL were used. In each gut sample, an area (0.1 mm^2) of a microscopic image from a similar gut region was randomly selected to count the number of AstA$^+$ cells (**e**). The gut is arranged from anterior to posterior, moving from top to bottom in the photo (**c**–**e**). Data are mean ± s.e.m. *P* values (**$p < 0.01$, ***$p < 0.001$, ns not significant) are indicated; one-way ANOVA with Tukey's post hoc test in (**c**–**g**). Nuclei were stained with DAPI in blue. Scale bar, 50 μm. Genotypes, sample sizes, and statistical analyses are shown in Supplementary Data 1. Source data are provided in the Source Data file.

experiments indicate that it can support larval growth under our experimental inhalation conditions (Supplementary Fig. 12), suggesting that other VSFs, besides (2R,3R)-2,3-butanediol, are likely involved in host growth promotion. Further in-depth investigation will be needed to fully understand the *Acetobacter*-derived VSFs and their signaling pathways.

It is striking to note that VSFs including (2R,3R)-2,3-butanediol are also emitted from the plant root microbiome (e.g., rhizobacteria such as *Bacillus subtilis* and *Bacillus amyloliquefaciens*)[65]. Importantly, *Bacillus*-emitted (2R,3R)-2,3-butanediol promotes plant growth and enhances crop yields[65]. Interestingly, we found that (2R,3R)-2,3-butanediol emitted from the plant root microbiome can also promote *Drosophila* larval growth (Supplementary Fig. 13). These results reveal striking similarities between animal and plant growth systems mediated by microbiome-emitted volatiles, although the exact molecular mechanism of (2R,3R)-2,3-butanediol-mediated plant growth (e.g., the receptor and its downstream signaling pathway in a plant system) remains to be elucidated. In addition to host growth promotion, what are the advantages of (2R,3R)-2,3-butanediol in host-microbe interactions? In the plant system, it has been reported that (2R,3R)-2,3-butanediol can trigger systemic resistance, possibly by boosting plant innate immunity[66]. Furthermore, (2R,3R)-2,3-butanediol is shown to be required for longer root colonization by augmenting bacterial resistance to the acidic environment around the plant root[67]. In this context, it would be interesting to examine whether (2R,3R)-2,3-butanediol is involved in bacterial ability for gut colonization or modulation of host innate immunity in the *Drosophila* system.

Another interesting point is that LP^{WJL}-mediated growth of malnourished hosts appears to be conserved from invertebrates to vertebrates. In a mammalian model of malnutrition, the cell wall component of LP^{WJL} acts as a ligand for the NOD2 receptor, which is necessary for crypt cell proliferation, production of IGF-1, and promotion of postnatal growth[13]. Given that deregulation of the microbiome is closely associated with the progression of malnutrition-associated disease phenotypes (e.g., stunting)[68,69], and that probiotics such as LP^{WJL} improves systemic host growth under chronic malnutrition[13,14], the discovery of (2R,3R)-2,3-butanediol as a growth-promoting factor may contribute significantly to understanding of the role of the microbiome in alleviating host malnutrition including humans. Interestingly, microbiome-derived metabolites have been shown to activate ORs expressed in mouse enterochromaffin cells, a subtype of EECs in the mammalian gut[70]. Further investigation into the presence of enterochromaffin cells responding to (2R,3R)-2,3-butanediol in the mammalian gut may provide novel insights into LP^{WJL}-host interactions.

Methods

Fly strains

Fly stocks obtained from the Bloomington stock center were: Bnl-Gal4 (stock no. 62607); Bnl-LexA (stock no. 81576); LexAop-rcd2-RFP, UAS-CD8GFP (stock no. 67093); Btl-LexA (stock no. 66620); CCHA2-Gal4 (stock no. 84602); AstAR2-Gal4 (stock no. 84594); OR42b-Gal4 (stock no. 9972); Btl-Gal4 (stock no. 78328); UAS-Yorkie-Active (stock no. 28817); Actin-Gal4 (stock no. 25708); ORCO$^{-/-}$ (stock no. 23130); Mex1-Gal4 (stock no. 91368); UAS-GCaMP7c (stock no. 79030) and UAS-mCD8GFP (stock no. 27399); UAS-nlsTimer-NA (stock no. 78056)[71]. Fly stocks obtained from the Vienna *Drosophila* Resource Center were: UAS-Bnl-RNAi (stock no. 5730); UAS-DILP2-RNAi (stock no. 102033); UAS-CCHA2-RNAi (stock no. 102257); UAS-AstA-RNAi (stock no. 103215); UAS-CCHA2R-RNAi (stock no. 100290); UAS-AstAR2-RNAi (stock no. 108648); UAS-Yorkie-RNAi (stock no. 104523); UAS-OR42b-RNAi (stock no. 101143) and UAS-Or83b-RNAi (stock no. 13386). Other fly stocks used were: Btl Gal4[72]; DILP2-Gal4[50]; Yorkie-GFP-KI[73]; Merlin-YFP[74]; AstA-Gal4[53]; and CCHA2$^{-/-}$[51].

Generation of transgenic and mutant flies

The gRNA sequences for each gene used in the experiment are listed in Supplementary Table 1. C-terminal epitope (3x FLAG)-tagged OR42b or OR42b^{DN} was generated using CRISPR/Cas9 genome editing. AstA$^{-/-}$ mutants were generated using the method developed by Kondo and Ueda[75]. OR42b$^{-/-}$ mutants were generated using a conventional CRISPR/Cas9 genome editing method. HA-epitope fused to the carboxy-terminus of DILP2 B-chain and FLAG-epitope fused to the amino terminus of DILP2 A-chain (referred to as DILP2-HF) (Fig. 2a) were generated using CRISPR/Cas9 genome editing. DILP3-HF and DILP5-HF were also generated using the same methods. HA- and FLAG-epitope tagging sites for DILPs were used exactly as described previously[76]. P-element-mediated germline transformations were carried out to generate UAS-OR42b^{DN} flies.

Fly rearing

The detailed fly genotypes used in this study are listed in the Supplementary Data 1. The flies were maintained at a temperature of 25 °C with a 12-h dark-light cycle on Bloomington Stock Center's standard cornmeal-agar medium.

Experiments involving the treatment with volatiles

Germ-free embryos were generated exactly as described previously[9] and maintained on a protein malnutrition diet [1% yeast (Lesaffre, France), 6.97% cornmeal (Sunglim Co., South Korea), 9.6% sucrose (Samyang Co., South Korea), 1.5% agar (Hansol Tech., South Korea), 0.03% Bokinin, and 0.5% propionic acid]. Germ-free embryos were treated by gases emitted from a bacterial plate (overnight cultured plate previously inoculated with 6×10^8 c.f.u. of bacterial cells) or from synthetic chemical compounds (0.3% or 0.03 %) in a chamber (Fig. 1a) throughout the development. Different bacterial strains including LP WJL strain (wild-type LP^{WJL} strain, LP^{WJL}ΔALS, and LP^{WJL}ΔALS_ALS), *Bacillus subtilis* 168 strain[77] (wild-type strain, *B. subtilis* ΔALS_S, *B. subtilis* ΔALS_D, and *B. subtilis* ΔPta) and *Bacillus amyloliquefaciens* FZB42 strain[78] (wild-type strain, *Bacillus amyloliquefaciens* △ALS_S,

https://doi.org/10.1038/s41467-025-57484-4

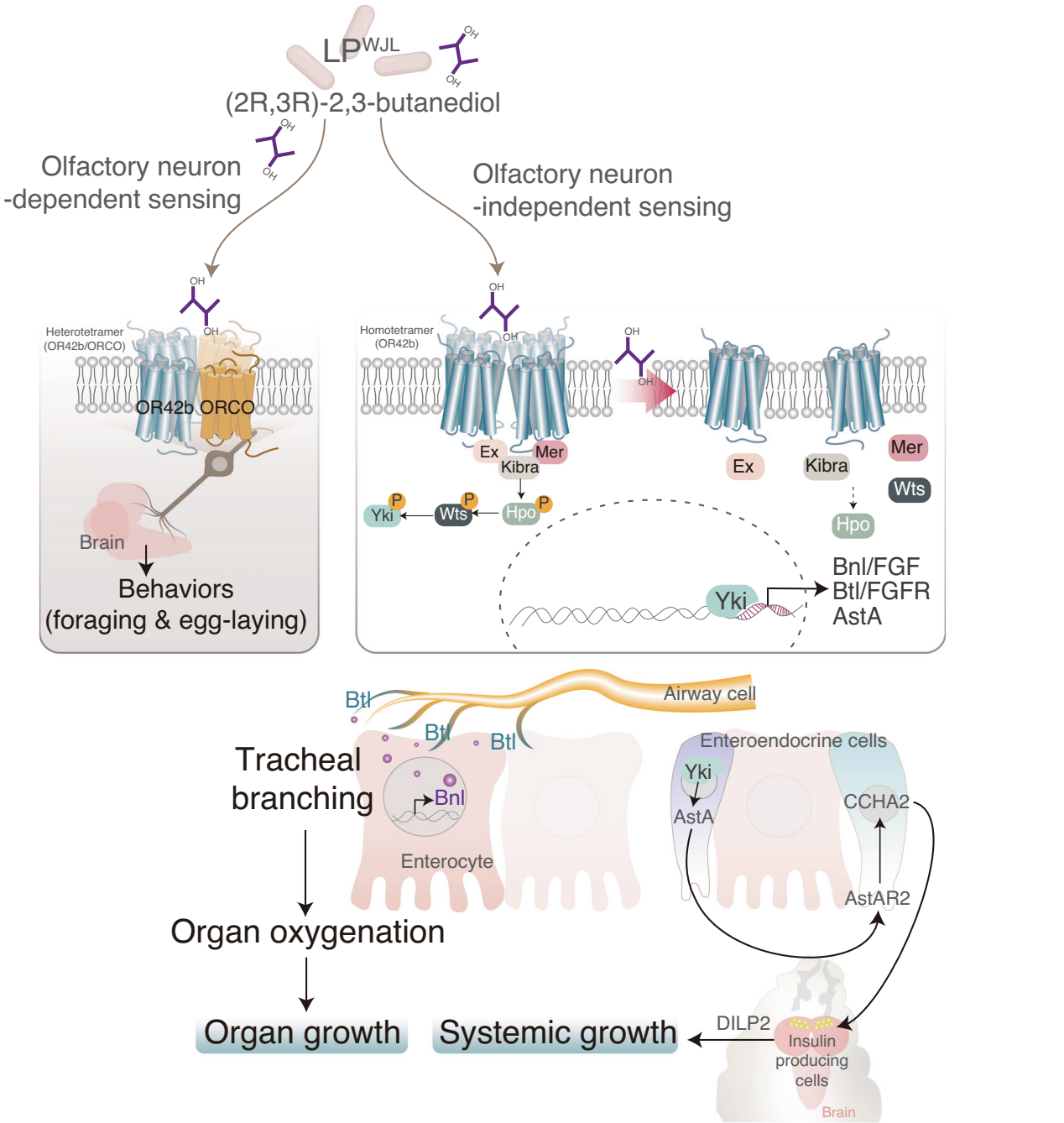

Fig. 8 | Model for the olfactory neuron-independent sensing of the microbiome-emitted (2R,3 R)-2,3-butanediol for the activation of somatotrophic airway-gut-brain axis. Traditional mechanism (i.e., olfactory neuron-dependent) of OR42b-mediated scent sensing (shown in the left panel) is based on the previous studies[18,31–34]. In this case, OR42b (shown in blue) expressed in olfactory neurons may form a heterotetramer (possibly two OR42b and two ORCO molecules) with co-receptor ORCO (shown in yellow). An olfactory neuron-independent mechanism of OR42b-mediated scent sensing discovered in the present study is shown in the right panel. In this case, OR42b (non-neuronally expressed in subsets of tracheal airway cells, EECs, and enterocytes) likely forms a homotetramer without the assistance of ORCO. In the absence of microbiome-emitted (2R,3R)-2,3-butanediol, Merlin (Mer) complex composed of Mer-kibra-Expanded (Ex) is tethered to the membrane-localized OR42b to sequentially activate Hippo (Hpo) kinase and Warts (Wts) kinase. Activated-Wts kinase phosphorylates Yorkie (Yki) for its cytoplasmic retention. Binding of (2R,3R)−2,3-butanediol to the OR42b initiates the dispersal of membrane-localized OR42b and Mer complex. Dispersed Mer complex inactivates Hpo-Wts kinases, resulting in Yki dephosphorylation for nuclear localization and target gene activation; *Branchless* (*Bnl*, a homolog of mammalian FGF) in the enterocytes, *Breathless* (*Btl*, a homolog of the mammalian FGF receptor) in the tracheal airway cells, and *Allatostatin A* (*AstA*) in the EECs. Bnl in enterocytes guides the migration of Btl^{+} tracheal airway cells during tracheal branching formation to deliver oxygen to the target organs for organ growth. Yki-dependent *AstA* expression in EECs induces CCHA2 peptide expression in AstA receptor-2 (AstAR2)-expressing EECs. CCHA2 peptide hormones in turn act on their receptors for DILP2 secretion from brain insulin-producing cells, thereby forming the somatotrophic gut-brain axis for systemic growth. CCHA2 peptide hormones in turn act on their receptors for DILP2 secretion from brain IPCs, thereby forming the somatotrophic gut-brain axis for systemic growth. Although the CCHA2 receptor (CCHA2R) has been shown to be expressed in larval IPCs[51], it remains to be elucidated whether gut-derived CCHA2 directly activates CCHA2R-expressing IPCs or indirectly activates IPCs (e.g., via CCHA2R-expressing enteric neurons).

and *Bacillus amyloliquefaciens* FZB42△ALS_D) were used. Body size or organ size was measured at 144 h AEL using a microscope (Zeiss; stemi 305) and was quantified using Zen 3.1 (blue edition) software.

Real-time PCR

Total RNA was extracted from 10 larval guts using the TRIzol reagent (Invitrogen). Real-time PCR was performed to quantify gene expression using the double-stranded DNA dye SYBR Green (Perkin Elmer). SYBR Green analysis was conducted using an ABI PRISM 7700 system (PE Applied Biosystems, Carlsbad, CA, USA) following the manufacturer's instructions. All samples were analyzed in triplicate, and the levels of detected mRNA were determined by cycling threshold analysis, followed by normalization using RP49 as a control. The relative expression of the target gene was determined. Primer pairs for detecting gene transcripts are listed in Supplementary Table 2.

Immunohistochemistry

Tissues were dissected in 1x PBS and then fixed for 30 min with 4% paraformaldehyde. The gut tissue samples were washed five times with 0.1% Triton X-100 PBS and incubated with 5% bovine serum albumin in 0.1% Triton X-100 PBS for 1 h. In the case of brain tissues, samples were washed five times with 0.3% Triton X-100 PBS and incubated with 5% bovine serum albumin in 0.3% Triton X-100 PBS (for brains) for 3 h. The samples were then washed five times with 1x PBS and incubated with the primary antibody overnight at 4 °C. Subsequently, the samples were washed five times for 5 min with 0.1% Triton X-100 in PBS (for midguts) or 0.3% Triton X-100 in PBS (for brains), followed by incubation with the secondary antibody for 1 h at room temperature. The samples were washed five times for 5 min with 0.1% Triton X-100 (for midguts) or 0.3% Triton X-100 (for brains) in PBS and then washed five times for 5 min with 1x PBS. Finally, the samples were mounted using a mounting buffer (Vectorshield, Vector Laboratories Inc., Burlingame, CA, USA) and analyzed by confocal microscopy (Carl Zeiss). The primary antibodies used in this study were rabbit anti-GFP (1:500; Invitrogen A11122), mouse anti-Prospero (1:100; DSHB AB_528440), mouse anti-DsRed (1:500; Santa Cruz Biology sc-390909), mouse anti-FLAG (1:500; Sigma-Aldrich F1804), rabbit anti-CCHA2 (1:500; newly generated for this study), mouse anti-dlg (1:500; DSHB AB_528203), and rabbit anti-AstA (1:500; Biorbyt). The secondary antibodies used were Fluor 568 goat anti-mouse IgG (1:500; Invitrogen A11004), Fluor 568 goat anti-rabbit IgG (1:500; Invitrogen A11011), Fluor 488 goat anti-mouse IgG (1:500; Invitrogen A11001), and Alexa Fluor 488 goat anti-rabbit IgG (1:500; Invitrogen A11008). Alexa Fluor 633 Phalloidin (1:30; Invitrogen A22284) and DAPI (1:1000; Roche 10236276001) were used for brush border membrane and nuclear staining, respectively.

Quantification of tracheal coverage

To quantify the tracheal coverage of midguts, images acquired by confocal microscopy (LSM700; Carl Zeiss) at 20× magnification were individually processed using ImageJ. The ROI in the gut was cropped to a size of 300 × 300 pixels. The values of tracheal coverage represent the percentage of the area occupied by the trachea per ROI (i.e., the number of pixels of the trachea per that of the ROI of the gut).

Quantification of oxygen concentration

The oxygen concentration of gut tissue was measured using two-color DsRed FT Timer protein, essentially as described previously[71]. Briefly, the signal intensities of both green and red fluorescence were measured using ZEN image software within an ROI with a size of 150 × 150 pixels. The red/green fluorescence ratio indicates oxygen concentration.

Quantification of Yorkie translocation

To quantify Yorkie translocations in midguts, images acquired using confocal microscopy (LSM700; Carl Zeiss) at 40× magnification were processed individually with Zen image software. To facilitate visualization of the cytoplasmic and nuclear regions of individual cells, Dlg, a septate junction marker, and DAPI were used for staining. The nucleus-to-cytoplasm GFP intensity ratio was then calculated by dividing the GFP intensity in the nucleus by that in the cytoplasm. Three to five cells were selected from each image to measure Yorkie translocations.

Generation of ALS deletion mutant of LP^{WJL} and LP^{NC8} strain

Homologous sequences of 1000 bp upstream and 1217 bp downstream of the ALS coding sequence were subcloned into the pGID 023 vector[79]. Subsequently, the constructed plasmid was transformed into LP via electroporation. A homologous recombination strategy was employed to generate the LP^{WJL}ΔALS, LP^{NC8}ΔALS, and LP^{NC8}Δdlt_ΔALS mutant strains. The mutant bacterial strains were confirmed via PCR and sequencing analysis. To generate a rescue strain (LP^{WJL}ΔAls_Als), the Als gene was cloned in the pBR 256 expression vector and then introduced into the LP^{WJL}ΔAls.

Measurement of circulating DILP2, 3 and 5

The HA and FLAG-tagged DILP2-HF, DILP3-HF, and DILP5-HF knock-in larvae were used to measure the circulating levels of DILP2, DILP3, and DILP5. In each sample, animals (a single larva or a pool of 10 larvae) were crushed in a tube containing 70 µL of PBS to obtain hemolymph. Solution (~70 µL) containing hemolymph was briefly centrifuged and an aliquot (50 µL) was used to quantify circulating DILP-HF level using a sandwich ELISA, as described previously[76]. FLAG-(GS)-HA peptide (D-Y-K-D-D-D-D-K-G-G-G-G-S-Y-P-Y-D-V-P-D-Y-A-amide) were synthesized (Anygen, South Korea) and used for a standard curve, as described previously[76]. Each value from a single larva was normalized by the volume of the respective larva.

Ex vivo calcium imaging using GCaMP

Ex vivo calcium imaging using GCaMP7c was performed essentially as described previously[80]. Larvae were dissected in the adult hemolymph-like (AHL) solution (108 mM NaCl, 8.2 mM $MgCl_2$, 4 mM $NaHCO_3$, 1 mM NaH_2PO_4, 2 mM $CaCl_2$, 5 mM KCl, 5 mM HEPES, 80 mM sucrose, pH 7.3). Tissues (trachea or gut) were immobilized using a mesh (Electron Microscopy Science; No. 100) in a magnetic chamber (Chamlide; CM-B18-1PA). The tracheal cells or gut cells bathed in the AHL solution were recorded for 5 min to establish a baseline. Subsequently, the solution was changed to AHL solution supplemented with 0.003% of each stereoisomer of 2,3-butanediol volatiles. Images were captured at a speed of 3 s per frame using LSM700 Carl Zeiss confocal microscopy.

Expression and purification of OR42b

The DNA encoding OR42b was PCR-amplified using a *Drosophila* cDNA library and subsequently subcloned into an EEV vector containing N-terminal Strep-tag II and EGFP. Baculovirus containing the Strep II-EGFP tagged OR42b sequence was created in SF9 cells (ATCC CRL-1711). Cells were grown in suspension at 37 °C in SF-900 II SFM medium (Gibco) supplemented with 10% (v/v) fetal bovine serum with 5% (v/v) carbon dioxide until they reached a density of 0.8 ~ 1.2 × 10^6 cells/mL and then infected at a multiplicity of infection of 1. After 48 h, 10 mM sodium butyrate (Sigma-Aldrich) was added to the medium and the temperature was reduced to 30 °C for the remainder of the incubation. The cells were harvested ~48 h after initial infection by centrifugation and were flash-frozen in liquid nitrogen. Pellets were stored at −80 °C until thawed for purification.

For the purification step, frozen cell pellets were thawed on ice and resuspended in 20 mL of lysis buffer per gram of cells. Lysis buffer was composed of 50 mM HEPES (pH 7.5), 375 mM NaCl, 1 µg/mL leupeptin, 1 µg/mL aprotinin, 1 µg/mL pepstatin A, 1 mM phenylmethylsulfonyl fluoride (PMSF) and ~0.1 mg/mL DNase I. After resuspending and grinding the pellet using a tissue grinder (Kimble), OR42b was extracted using 2% (w/v) lauryl maltose neopentyl glycol (LMNG; Anatrace) for 2 h at 4 °C under constant stirring with a magnetic bar. After centrifugation at 20,000 × *g*, the supernatant was added to 0.2 mL StrepTactin Sepharose resin (GE Healthcare) and rolled at 4 °C for 2 h. The resin was collected and washed with 10 column volumes of 20 mM HEPES/ NaOH, and 150 mM NaCl with 0.01% (w/v) LMNG. OR42b was eluted by adding 2.5 mM desthiobiotin (DTB). The eluted sample was injected onto a Superose 6 Increase column (GE Healthcare) equilibrated in 20 mM HEPES/ NaOH, 150 mM NaCl with 0.004% (w/v) LMNG.

Negative staining electron microscopy imaging

The eluted sample (5 µL) from StrepTactin Sepharose resin was applied to glow-discharged holey carbon grids with a thin layer of carbon. After adsorption for 1 min, the sample was stained with two droplets of 1% (w/v) uranyl formate solution and water, blotted gently to remove the residual stain, and air-dried. Specimens were examined under the JEOL 2100 Plus electron microscope equipped with RIO9 Camera and operated at 200 kV acceleration voltage, under a nominal magnification of 40,000 and pixel size of 1.3 Å. A total of 230 particles were manually selected from 10 micrographs and averaged to 2D classification using RELION3[81].

AlphaFold prediction and sequence comparison of OR42b

The monomeric and tetrameric structure of OR42b were predicted based on the protein sequence by AlphaFold and AlphaFold multimer using the ColabFold website[82–84]. Clustal Omega was used for the sequence alignment of OR42b and *Machilis hrabei* OR5[85].

Odorant-binding pocket determination using SwissDock

The monomeric OR42b, predicted by AlphaFold[82], was used to investigate the binding of the agonist. Mol2 files for (2R,3R)-2,3-butanediol were obtained from the Zinc database[86]. Both the monomeric OR42b and the (2R,3R)-2,3-butanediol files were used as inputs in the web-based SwissDock program[87]. Initially, a blind docking process was performed to identify potential binding pockets for the agonist. Subsequently, (2R,3R)-2,3-butanediol was used to identify both the outer and inner binding sites of OR42b. The quality and pose scores of each binding were assessed based on Full Fitness and ΔG (kcal/mol). The docking poses of each molecule were visually analyzed using UCSF Chimera[88].

Analysis of volatile organic compounds by HS-GC/MS

The quantitative analysis of three volatile organic compounds [3-hydroxy-2-butanone, diacetyl, and (2R,3R)-2,3-butanediol] was carried out using headspace (HS) sampler, combined with GC-MS (Shimadzu Corporation, Kyoto, Japan), which was equipped at the Ewha Drug Development Research Core Center. A total volume of 1 mL of each sample was added to separate 20 mL glass headspace vials and immediately capped with a septum-attached metal screw cap to minimize any loss of volatile analytes. Each vial was then transferred into the HS instrument from a rotating carousel. The HS unit was independently controlled by GC and MS, and the overall operation involved three fundamental steps: equilibration, pressurization, and sample transfer/loading to the loop. The optimized HS method was based on an oven temperature of 80°C and a sample/transfer line temperature of 180 °C. Under this condition, vials were equilibrated for 15 min, and subsequently pressurized at 50 kPa for 2 min with high-purity helium (He) gas. Pressurized sample gas in the vial was then transferred to the loop for 0.5 min (loading time) and finally fed into the GC for another 1 min (injection time). Subsequent GC separation was conducted using a 30 m × 0.25 mm i.d., 0.25 µm Stabilwax-MS capillary column with high-purity He at a flow rate of 1 mL/min as the carrier gas (mobile phase). GC oven was initially held at 40 °C for 5 min, then increased by 60 °C/min to 160 °C and held for 3 min. The temperature was once again ramped to 200 °C at a rate of 20 °C/min and held for an additional 5 min. The injection port of GC was maintained at 220 °C in split mode, with a ratio of 1:10. Samples were finally detected via MS under an electron ionization mode. The ion source temperature was set to 220 °C, and the detector voltage was adjusted relative to the tuning results. Final data were obtained in selected ion monitoring (SIM) mode. The ions selected for SIM were: *m/z* 41, 42, 43, 44, 50, and 86 for diacetyl; *m/z* 27, 29, 45, 43, and 88 for 3-hydroxy-2-butanone; *m/z* 45, 47, 55, 57, and 90 for (2R,3R)-2,3-butanediol. Chemical identification and quantitation of each separated peak were conducted with LabSolution software provided by Shimadzu Co.

Olfactory preference assay

The olfactory preference assay in *Drosophila* was conducted essentially as described previously[89], with minor modifications. For the larvae, 20 third-instar larvae were positioned at the center of a petri dish with a diameter of 9 cm. Two different attractants were placed at opposite positions on its periphery. The preference assay was conducted for a period of 5 min. The number of larvae near each attractant was counted. For the adults, fifty 5-day-old female flies were introduced into a container containing two trap vials with different attractants for a period of 16 h. The preference index was calculated from a choice between water and 2,3-butanediol (3% v/v), or between parental LPWJL wildtype and its acetolactate synthase mutant lacking 2,3-butanediol production (~1.8×10^9 c.f.u. each).

Quantification of food intake

The food intake assay was conducted essentially as described previously[90]. Germ-free embryos were placed on a protein malnutrition diet containing 2.5% (w/v) blue food dye (FD&C Blue Dye No.1), and were treated either without or with inhalation of LP^{WJL} volatiles during entire larval stages. At 24, 48, 72, and 96 h AEL, larvae were washed with autoclaved water to eliminate any residual dye present on their outer surface. In each measurement, three larvae were homogenized in 70 µL of autoclaved water and subsequently centrifuged for 60 s at 16,000 × *g*. The supernatant (50 µL) was used to measure the absorbance at 629 nm using the Flexstation3 Multi-Mode Microplate Reader (Molecular Devices, LLC).

Statistics and reproducibility

Experiment was repeated independently three times (Figs. 3d, 4f, g, 5a–d and 7c), four times (Figs. 1f and 3a, e), or five times (Fig. 2b), and one representative image was shown. For the 2D class images (Fig. 2c), an average was generated using 200 particles from 10 micrographs. Statistical analysis in this study was performed using GraphPad Prism 9.0. Comparisons between the two samples were conducted using an unpaired two-tailed *t*-test. For comparisons involving multiple samples, one-way ANOVA with Tukey's post hoc test or two-way ANOVA with Tukey's multiple comparison was employed.

Reporting summary

Further information on research design is available in the Nature Portfolio Reporting Summary linked to this article.

Data availability

Data generated and used in this study are described within the Article, Supplementary Data files, Supplementary Information, and Source Data file. Source data are provided with this paper.

References

1. Rooks, M. G. & Garrett, W. S. Gut microbiota, metabolites and host immunity. *Nat. Rev. Immunol.* **16**, 341–352 (2016).
2. Sommer, F. & Bäckhed, F. The gut microbiota—masters of host development and physiology. *Nat. Rev. Microbiol.* **11**, 227–238 (2013).
3. Heijtza, R. D. et al. Normal gut microbiota modulates brain development and behavior. *Proc. Natl Acad. Sci. USA* **108**, 3047–3052 (2011).
4. Lee, W.-J. & Hase, K. Gut microbiota-generated metabolites in animal health and disease. *Nat. Chem. Biol.* **10**, 416–424 (2014).
5. Kim, B. et al. Response of the microbiome–gut–brain axis in Drosophila to amino acid deficit. *Nature* **593**, 570–574 (2021).
6. Lee, W. J. & Brey, P. T. in *Annual Review of Cell and Developmental Biology* Vol. 29 (ed. Schekman, R.) 571–592 (Annual Reviews, 2013).
7. Buchon, N., Broderick, N. A. & Lemaitre, B. Gut homeostasis in a microbial world: insights from Drosophila melanogaster. *Nat. Rev. Microbiol.* **11**, 615–626 (2013).
8. Douglas, A. E. Simple animal models for microbiome research. *Nat. Rev. Microbiol.* **17**, 764–775 (2019).
9. Ryu, J. H. et al. Innate immune homeostasis by the homeobox gene caudal and commensal-gut mutualism in Drosophila. *Science* **319**, 777–782 (2008).
10. Ludington, W. B. & Ja, W. W. Drosophila as a model for the gut microbiome. *PLoS Pathog.* **16**, e1008398 (2020).
11. Shin, S. C. et al. Drosophila microbiome modulates host developmental and metabolic homeostasis via insulin signaling. *Science* **334**, 670–674 (2011).
12. Storelli, G. et al. Lactobacillus plantarum promotes Drosophila systemic growth by modulating hormonal signals through TOR-dependent nutrient sensing. *Cell Metab.* **14**, 403–414 (2011).
13. Schwarzer, M. et al. Microbe-mediated intestinal NOD2 stimulation improves linear growth of undernourished infant mice. *Science* **379**, 826–833 (2023).
14. Schwarzer, M. et al. Lactobacillus plantarum strain maintains growth of infant mice during chronic undernutrition. *Science* **351**, 854–857 (2016).
15. Ezenwa, V. O., Gerardo, N. M., Inouye, D. W., Medina, M. & Xavier, J. B. Animal behavior and the microbiome. *Science* **338**, 198–199 (2012).
16. Teseo, S. et al. The scent of symbiosis: gut bacteria may affect social interactions in leaf-cutting ants. *Anim. Behav.* **150**, 239–254 (2019).
17. Vernier, C. L. et al. The gut microbiome defines social group membership in honey bee colonies. *Sci. Adv.* **6**, https://doi.org/10.1126/sciadv.abd3431 (2020).
18. Wong, A. C. N. et al. Gut microbiota modifies olfactory-guided microbial preferences and foraging decisions in Drosophila. *Curr. Biol.* **27**, 2397 (2017).
19. Couto, A., Alenius, M. & Dickson, B. J. Molecular, anatomical, and functional organization of the Drosophila olfactory system. *Curr. Biol.* **15**, 1535–1547 (2005).
20. De Bruyne, M. & Baker, T. C. Odor detection in insects: volatile codes. *J. Chem. Ecol.* **34**, 882–897 (2008).
21. Vosshall, L. B., Amrein, H., Morozov, P. S., Rzhetsky, A. & Axel, R. A spatial map of olfactory receptor expression in the Drosophila antenna. *Cell* **96**, 725–736 (1999).
22. Kreher, S. A., Kwon, J. Y. & Carlson, J. R. The molecular basis of odor coding in the Drosophila larva. *Neuron* **46**, 445–456 (2005).
23. Guo, H., Kunwar, K. & Smith, D. Odorant receptor sensitivity modulation in Drosophila. *J. Neurosci.* **37**, 9465–9473 (2017).
24. Mathew, D. et al. Functional diversity among sensory receptors in a Drosophila olfactory circuit. *Proc. Natl. Acad. Sci. USA* **110**, E2134–E2143 (2013).
25. Maßberg, D. & Hatt, H. Human olfactory receptors: novel cellular functions outside of the nose. *Physiol. Rev.* **98**, 1739–1763 (2018).
26. Kang, N. & Koo, J. Olfactory receptors in non-chemosensory tissues. *BMB Rep.* **45**, 612 (2012).
27. Joseph, R. M. & Carlson, J. R. Drosophila chemoreceptors: a molecular interface between the chemical world and the brain. *Trends Genet.* **31**, 683–695 (2015).
28. Krause, S. A., Overend, G., Dow, J. A. & Leader, D. P. FlyAtlas 2 in 2022: enhancements to the Drosophila melanogaster expression atlas. *Nucleic Acids Res.* **50**, D1010–D1015 (2022).
29. Harrop, T. W., Pearce, S. L., Daborn, P. J. & Batterham, P. Whole-genome expression analysis in the third instar larval midgut of Drosophila melanogaster. *G3 Genes, Genomes, Genet.* **4**, 2197–2205 (2014).
30. Wang, M. et al. High-resolution 3D spatiotemporal transcriptomic maps of developing Drosophila embryos and larvae. *Dev. Cell* **57**, 1271–1283. e1274 (2022).
31. Goldman-Huertas, B. et al. Evolution of herbivory in Drosophilidae linked to loss of behaviors, antennal responses, odorant receptors, and ancestral diet. *Proc. Natl. Acad. Sci. USA* **112**, 3026–3031 (2015).
32. Stökl, J. et al. A deceptive pollination system targeting drosophilids through olfactory mimicry of yeast. *Curr. Biol.* **20**, 1846–1852 (2010).
33. Fischer, C. N. et al. Metabolite exchange between microbiome members produces compounds that influence Drosophila behavior. *eLife* **6**, e18855 (2017).
34. De Bruyne, M., Smart, R., Zammit, E. & Warr, C. G. Functional and molecular evolution of olfactory neurons and receptors for aliphatic esters across the Drosophila genus. *J. Comp. Physiol. A* **196**, 97–109 (2010).
35. Bueno, E. et al. Response of wild spotted wing drosophila (Drosophila suzukii) to microbial volatiles. *J. Chem. Ecol.* **46**, 688–698 (2020).
36. Yan, H. et al. Evolution, developmental expression and function of odorant receptors in insects. *J. Exp. Biol.* **223**, https://doi.org/10.1242/jeb.208215 (2020).
37. Del Mármol, J., Yedlin, M. A. & Ruta, V. The structural basis of odorant recognition in insect olfactory receptors. *Nature* **597**, 126–131 (2021).
38. Ghabrial, A., Luschnig, S., Metzstein, M. M. & Krasnow, M. A. Branching morphogenesis of the Drosophila tracheal system. *Annu. Rev. Cell Dev. Biol.* **19**, 623–647 (2003).
39. Jarecki, J., Johnson, E. & Krasnow, M. A. Oxygen regulation of airway branching in Drosophila is mediated by branchless FGF. *Cell* **99**, 211–220 (1999).
40. Ohshiro, T., Emori, Y. & Saigo, K. Ligand-dependent activation of breathless FGF receptor gene in Drosophila developing trachea. *Mech. Dev.* **114**, 3–11 (2002).
41. Klambt, C., Glazer, L. & Shilo, B. Z. Breathless, a Drosophila FGF receptor homolog, is essential for migration of tracheal and specific midline glial-cells. *Genes Dev.* **6**, 1668–1678 (1992).
42. Ohshiro, T. & Saigo, K. Transcriptional regulation of breathless FGF receptor gene by binding of TRACHEALESS/dARNT heterodimers to three central midline elements in Drosophila developing trachea. *Development* **124**, 3975–3986 (1997).
43. Sutherland, D., Samakovlis, C. & Krasnow, M. A. Branchless encodes a Drosophila FGF homolog that controls tracheal cell migration and the pattern of branching. *Cell* **87**, 1091–1101 (1996).
44. Linneweber, G. A. et al. Neuronal control of metabolism through nutrient-dependent modulation of tracheal branching. *Cell* **156**, 69–83 (2014).

45. Texada, M. J. et al. A fat-tissue sensor couples growth to oxygen availability by remotely controlling insulin secretion. *Nat. Commun.* **10**, 1955 (2019).
46. Lee, B., Barretto, E. C. & Grewal, S. S. TORC1 modulation in adipose tissue is required for organismal adaptation to hypoxia in Drosophila. *Nat. Commun.* **10**, 1878 (2019).
47. Brogiolo, W. et al. An evolutionarily conserved function of the Drosophila insulin receptor and insulin-like peptides in growth control. *Curr. Biol.* **11**, 213–221 (2001).
48. Koyama, T., Texada, M. J., Halberg, K. A. & Rewitz, K. Metabolism and growth adaptation to environmental conditions in Drosophila. *Cell. Mol. Life Sci.* **77**, 4523–4551 (2020).
49. Colombani, J. et al. A nutrient sensor mechanism controls Drosophila growth. *Cell* **114**, 739–749 (2003).
50. Ikeya, T., Galic, M., Belawat, P., Nairz, K. & Hafen, E. Nutrient-dependent expression of insulin-like peptides from neuroendocrine cells in the CNS contributes to growth regulation in Drosophila. *Curr. Biol.* **12**, 1293–1300 (2002).
51. Sano, H. et al. The nutrient-responsive hormone CCHamide-2 controls growth by regulating insulin-like peptides in the brain of Drosophila melanogaster. *PLoS Genet.* **11**, e1005209 (2015).
52. Wegener, C. & Chen, J. Allatostatin A signalling: progress and new challenges from a paradigmatic pleiotropic invertebrate neuropeptide family. *Front. Physiol.* **13**, 920529 (2022).
53. Hergarden, A. C., Tayler, T. D. & Anderson, D. J. Allatostatin-A neurons inhibit feeding behavior in adult Drosophila. *Proc. Natl Acad. Sci. USA* **109**, 3967–3972 (2012).
54. Li, Y. et al. Metabolic control of progenitor cell propagation during Drosophila tracheal remodeling. *Nat. Commun.* **13**, 2817 (2022).
55. Baumgartner, R., Poernbacher, I., Buser, N., Hafen, E. & Stocker, H. The WW domain protein Kibra acts upstream of Hippo in Drosophila. *Dev. Cell* **18**, 309–316 (2010).
56. Yu, J. et al. Kibra functions as a tumor suppressor protein that regulates Hippo signaling in conjunction with Merlin and Expanded. *Dev. Cell* **18**, 288–299 (2010).
57. Oh, H. & Irvine, K. D. In vivo regulation of Yorkie phosphorylation and localization. *Development* **135**, 1081–1088 (2008).
58. Hsiao, E. Y. et al. Microbiota modulate behavioral and physiological abnormalities associated with neurodevelopmental disorders. *Cell* **155**, 1451–1463 (2013).
59. Bercik, P. et al. The intestinal microbiota affect central levels of brain-derived neurotropic factor and behavior in mice. *Gastroenterology* **141**, 599–U701 (2011).
60. Engel, P., Martinson, V. G. & Moran, N. A. Functional diversity within the simple gut microbiota of the honey bee. *Proc. Natl. Acad. Sci. USA* **109**, 11002–11007 (2012).
61. Theis, K. R., Schmidt, T. M. & Holekamp, K. E. Evidence for a bacterial mechanism for group-specific social odors among hyenas. *Sci. Rep.* **2**, 8 (2012).
62. Brand, P. et al. The origin of the odorant receptor gene family in insects. *eLife* **7**, e38340 (2018).
63. Kamareddine, L., Robins, W. P., Berkey, C. D., Mekalanos, J. J. & Watnick, P. I. The immune deficiency pathway modulates enteroendocrine function and host metabolism. *Cell Metab.* **28**, 449 (2018).
64. Matos, R. C. et al. D-Alanylation of teichoic acids contributes to -mediated growth during chronic undernutrition. *Nat. Microbiol.* **2**, 1635–1647 (2017).
65. Ryu, C.-M. et al. Bacterial volatiles promote growth in Arabidopsis. *Proc. Natl. Acad. Sci. USA* **100**, 4927–4932 (2003).
66. Ryu, C.-M. et al. Bacterial volatiles induce systemic resistance in Arabidopsis. *Plant Physiol.* **134**, 1017–1026 (2004).
67. Yi, H.-S. et al. Impact of a bacterial volatile 2, 3-butanediol on Bacillus subtilis rhizosphere robustness. *Front. Microbiol.* **7**, 993 (2016).
68. Subramanian, S. et al. Persistent gut microbiota immaturity in malnourished Bangladeshi children. *Nature* **510**, 417–421 (2014).
69. Gehrig, J. L. et al. Effects of microbiota-directed foods in gnotobiotic animals and undernourished children. *Science* **365**, eaau4732 (2019).
70. Bellono, N. W. et al. Enterochromaffin cells are gut chemosensors that couple to sensory neural pathways. *Cell* **170**, 185–198.e16 (2017).
71. Lidsky, P. V. et al. A genetically encoded fluorescent probe for imaging of oxygenation gradients in living Drosophila. *Development* **145**, dev156257 (2018).
72. Shiga, Y., Tanaka-Matakatsu, M. & Hayashi, S. A nuclear GFP/β-galactosidase fusion protein as a marker for morphogenesis in living Drosophila. *Dev. Growth Differ.* **38**, 99–106 (1996).
73. Borreguero-Muñoz, N. et al. The Hippo pathway integrates PI3K–Akt signals with mechanical and polarity cues to control tissue growth. *PLoS Biol.* **17**, e3000509 (2019).
74. Su, T., Ludwig, M. Z., Xu, J. & Fehon, R. G. Kibra and Merlin activate the Hippo pathway spatially distinct from and independent of expanded. *Dev. Cell* **40**, 478–490.e473 (2017).
75. Kondo, S. & Ueda, R. Highly improved gene targeting by germline-specific Cas9 expression in Drosophila. *Genetics* **195**, 715–721 (2013).
76. Park, S. et al. A genetic strategy to measure circulating Drosophila insulin reveals genes regulating insulin production and secretion. *PLoS Genet.* **10**, e1004555 (2014).
77. Cruz Ramos, H. et al. Fermentative metabolism of Bacillus subtilis: physiology and regulation of gene expression. *J. Bacteriol.* **182**, 3072–3080 (2000).
78. Chen, X. H. et al. Comparative analysis of the complete genome sequence of the plant growth–promoting bacterium Bacillus amyloliquefaciens FZB42. *Nat. Biotechnol.* **25**, 1007–1014 (2007).
79. Hols, P., Ferain, T., Garmyn, D., Bernard, N. & Delcour, J. Use of homologous expression-secretion signals and vector-free stable chromosomal integration in engineering of Lactobacillus plantarum for alpha-amylase and levanase expression. *Appl. Environ. Microbiol.* **60**, 1401–1413 (1994).
80. Oh, Y. et al. Periphery signals generated by Piezo-mediated stomach stretch and Neuromedin-mediated glucose load regulate the Drosophila brain nutrient sensor. *Neuron* **109**, 1979–1995.e1976 (2021).
81. Zivanov, J. et al. New tools for automated high-resolution cryo-EM structure determination in RELION-3. *eLife* **7**, e42166 (2018).
82. Jumper, J. et al. Highly accurate protein structure prediction with AlphaFold. *Nature* **596**, 583–589 (2021).
83. Evans, R. et al. Protein complex prediction with AlphaFold-Multimer. *biorxiv*, 2021.2010. 2004.463034 (2021).
84. Mirdita, M. et al. ColabFold: making protein folding accessible to all. *Nat. Methods* **19**, 679–682 (2022).
85. Sievers, F. et al. Fast, scalable generation of high-quality protein multiple sequence alignments using Clustal Omega. *Mol. Syst. Biol.* **7**, 539 (2011).
86. Irwin, J. J. et al. ZINC20—a free ultralarge-scale chemical database for ligand discovery. *J. Chem. Inf. Model.* **60**, 6065–6073 (2020).
87. Grosdidier, A., Zoete, V. & Michielin, O. SwissDock, a protein-small molecule docking web service based on EADock DSS. *Nucleic Acids Res.* **39**, W270–W277 (2011).
88. Pettersen, E. F. et al. UCSF Chimera—a visualization system for exploratory research and analysis. *J. Comput. Chem.* **25**, 1605–1612 (2004).
89. Ebrahim, S. A. et al. Drosophila avoids parasitoids by sensing their semiochemicals via a dedicated olfactory circuit. *PLoS Biol.* **13**, e1002318 (2015).
90. Wong, R., Piper, M. D., Wertheim, B. & Partridge, L. Quantification of food intake in Drosophila. *PLoS ONE* **4**, e6063 (2009).

Acknowledgements
We thank the W.-J.L. laboratory members for the discussion and critical reading of the manuscript. This work is supported by the National Research Foundation of South Korea (RS-2024-00345184 and RS-2022-NR067345).

Author contributions
Conceptualization: J.W.L., K.A.L., W.J.L.; investigation: J.W.L., K.A.L., I.H.J., J.H.L., K.N., M.K., K.C.C., S.H.K., Y.H.K., H.L., J.P., S.Y.H., Y.W.C., H.Y., E.K.K.; data analysis: J.W.L., K.A.L., Y.K., S.H.R., J.H.R., C.M.R., W.J.L.; supervision: W.J.L.; writing—original draft: J.W.L., K.A.L., W.J.L.; writing—review and editing: J.W.L., K.A.L., W.J.L.

Competing interests
The authors declare no competing interests.

Additional information
Supplementary information The online version contains supplementary material available at https://doi.org/10.1038/s41467-025-57484-4.

Correspondence and requests for materials should be addressed to Won-Jae Lee.

Peer review information *Nature Communications* thanks François Leulier, who co-reviewed with Longwei Bai and the other, anonymous, reviewer(s) for their contribution to the peer review of this work. A peer review file is available.